Characterising the internal structural complexity of the Southern North Sea Zechstein Supergroup Evaporites

Hector George Barnett[1], Mark T. Ireland[1], Cees Van der Land[1]

[1] Earth Ocean and Planetary Science Group, School of Natural and Environmental Sciences, Newcastle University, Newcastle Upon-Tyne NE1 7RU

Corresponding author: h.barnett2@ncl.ac.uk

Hector Barnett's PhD is funded through the Centre for Doctoral Training (CDT) in Geoscience and the Low Carbon Energy Transition. Seismic and well data were provided by the North Sea Transition Authority under an Open Government Licence. Bathymetry data was provided by The European Marine Observation and Data Network. Data were interpreted using Schlumberger's Petrel and Techlog software which was provided under an academic licence. The interpretations that underpin this study are available through data.ncl.ac.uk [Permant link to be added]

i. ABSTRACT

The internal complexity present within layered evaporite sequences is often an overlooked feature in sedimentary basins, with attention frequently concentrating on the external geometries that salt bodies form. Through the availability of large areas of 3D seismic data and new seismic imaging techniques the opportunity to view the internal structures that form within layered evaporites allows for a comprehensive characterisation of the different structural facies that may be present.

The key focus of this paper concentrates on the Zechstein evaporite deposits within the Southern North Sea of the United Kingdom's Continental Shelf. This analysis of the internal structural complexity and stratigraphical heterogeneity utilises 25,000 km^2 of existing 3D seismic data together with over 96 wells from the Southern North Sea. Characterisation of the different structural facies present was undertaken alongside mapping the spatial distribution to understand the relationship they have with one another and the deformation pathways that may have been taken. Layered evaporite sequences are an important component of geo-storage systems, either for cavern emplacement or sealing carbon storage reservoirs.

This work has shown; 1) there are contrasting internal geometries between different structural salt facies; 2) the internal heterogeneity is indicative of variations in the vertical strength profile of layered evaporite sequences; 3) the ability to possibly predict the internal heterogeneity of areas of poorly imaged salt, such as within salt structures, from surrounding structural facies of the salt; These findings suggest that there is significant internal complexity even within areas of the basin with minor salt mobilization and as such are important to consider in the assessment of geo-storage sites.

KEYWORDS: evaporites, structural geology, Zechstein, 3D seismic, salt cavern, hydrogen storage, energy transition

Vi. MAIN TEXT

1. INTRODUCTION

Layered evaporite sequences (LES) are common features of many sedimentary basins around the world (Butler et al., 2015), notable examples include the Zechstein Supergroup of Northern Europe, the Messinian of the Mediterranean and the Khuff of the Arabian Basin (Jackson and Hudec, 2017). LES are rarely composed of pure halite and typically have interbeds of other evaporite minerals and none evaporite lithologies (Rowan et al., 2019). The mechanical behaviour of LES is partly controlled by the proportion and layering order of the constituent lithologies present (Adamuszek et al., 2021). Interbeds, such as carbonates and anhydrites, are much stronger in both compressive and extensional regimes than halite (Table 1.), which undergoes flow at stresses of < 5 Mpa (Zulauf et al., 2011). These mechanically strong lithologies present within mobile evaporite layers can modify the behaviour of the internal structure and the level of deformation that can occur to LES (Strozyk et al., 2014). Differing quantities and distributions of mechanically strong interbeds influence the deformation and how internal strain is partitioned in mobile evaporites (Rowan et al., 2019). These mechanically strong units can also undergo a combination of ductile and brittle deformation (Strozyk et al., 2014), and help define and identify the strain and kinematic history of the LES (Zulauf and Zulauf, 2005).

While previous work e.g. (Evans and Jackson, 2021, Jackson et al., 2015) has identified the presence of intra-salt deformation, there has been limited emphasis on distinguishing the different styles and distribution of deformation and the implications for the processes that result in the observed geometries. In some cases (e.g. Jones and Davison, 2014, Hanafi et al., 2022) the ability to distinguish the internal deformation of LES is limited by the quality of the seismic data available. Often LES are described as having a chaotic or transparent appearance (Evans and Jackson, 2021), however, improvements in seismic processing sequences are leading to coherent reflectivity within these LES (Kirkham and Cartwright, 2021), potentially leading to a paradigm change in the view of the internal structural heterogeneity of LES.

Much of the current understanding of LES has come from their association with prolific hydrocarbon provinces, such as the Gulf of Mexico (Weimer et al., 2017), the Nile Delta (Aal et al., 2000), the South Atlantic conjugate margins (Wen et al., 2019) and the North Sea (Peryt et al., 2010), where sequences are important for both trapping geometries and seals (Archer et al., 2012, Sarg, 2001). Similarly, LES have been utilised for the development of underground caverns storing principally oil and natural gas (Tarkowski and Czapowski, 2018). It is likely that LES will be important components of geological storage systems (Kernen et al., 2021) as they can be utilised for the development of salt caverns for energy storage, for example, with hydrogen (Caglayan et al., 2020), or act as highly effective sealing lithologies for the geological sequestration of carbon dioxide (Miocic et al., 2014). A detailed characterisation of the internal complexity of LES is essential to understanding the variation in geomechanical and geochemical properties, which is vital for seal integrity and cavern stability (Lux, 2009).

This study uses observations and interpretations from 3D seismic and well data from the Southern North Sea to examine the style and distribution of the internal deformation within the LES of the Zechstein. The findings here have implications for understanding the deformation within LES more broadly and with applications in site characterisation for geological storage.

2. GEOLOGICAL SETTING

The Zechstein of Northern Europe is an expansive group of layered evaporites that was formed in the Late-Permian. The Zechstein has been studied extensively throughout the North Sea due to its importance in petroleum systems (Glennie, 1998). On the United Kingdom Continental Shelf (UKCS), the Zechstein is most commonly either the sealing sequence for the underlying Rotliegend natural gas reservoirs of the Southern North Sea (SNS) (Bailey et al., 1993) or has led to the formation of structural trapping geometries for Triassic-aged oil reservoirs in the Northern North Sea (Jackson and Stewart, 2017).

2.1 Tectonic evolution

There are two major east-west trending rift basins present on the eastern side of the UKCS: the North Permian Basin and the South Permian Basin (Figure. 1). The two basins, positioned north and south of one another, are separated by the Mid-North Sea High and the Ringkobing-flyn High (Clark et al., 1998). These two larger basins host numerous smaller sub-basins, such as the Forth Approaches Basin (Cartwright et al., 2001) and the Silver Pit Basin (Bailey et al., 1993), located in the North and South Permian Basins, respectively.

The South Permian Basin of the UKCS has developed over a period of 380 million years consisting of a complex geological history with several rift and post-rift phases. Rifting initiated with the collapse of the Late – Devonian aged Variscan Orogeny (Schulmann et al., 2014, Pharaoh et al., 2010) and subsequent late-Carboniferous inversion (Hodgson et al., 1992, Ziegler, 1990). Early-Permian rifting saw the two Permian basins of the North Sea open up and begin to develop (Hodgson et al., 1992, Glennie et al., 2003), this phase of rifting which lasted till the mid-Jurassic, was only briefly interrupted by post-rift thermal subsidence in the late-Permian (Hodgson et al., 1992, Geluk, 2007, Pharaoh et al., 2010). Tensional stresses that developed during the Triassic rifting led to the extension of both pre-existing faults and the evolution of systems, including the East Irish Sea (Glennie and Underhill, 1998, Zanella and Coward, 2003). By the mid-Jurassic, the tectonic regime had changed again, dominated by thermal doming and uplift (Zanella and Coward, 2003, Pharaoh et al., 2010). However, this event was short-lived, lasting only until the late-Jurassic where it was replaced by another phase of rifting (Thomas and Coward, 1996). When rifting ceased in the mid-Cretaceous, the basin experienced a short-term period of thermal subsidence, which lasted until the late-Cretaceous (Pharaoh et al., 2010), followed by a period of tectonic inversion which initiated in the Campanian (Erratt et al., 1999) and continued through to the early Cenozoic. As inversion ended, it was replaced by thermal subsidence once again; as the Cenozoic became incorporated into the North Sea thermal Sag basin, leading to up 3 km of Cenozoic sedimentation in areas (Ziegler, 1990, Wong et al., 2007).

2.2 Zechstein

Prior to the deposition of the Zechstein supergroup evaporites (ZSGE), the Permian-aged Rotliegend aeolian sediments were deposited during the early phases of thermal subsidence (Maynard and Gibson, 2001). During this phase of aeolian sedimentation, the basin was entirely landlocked, isolated from all surrounding ocean bodies (Peryt et al., 2010). Subsidence of the basin was greater than that of the rate of sedimentation, leading to an underfilled basin (Glennie et al., 2003). The basin remained underfilled into the late Permian due to the continued Permo-Triassic subsidence; this led to the centre of the basin being as low as 300m below average sea level by the late-Permian, and the onset of the ZSGE deposition (Glennie, 1998).

The Zechstein Ocean formed due to the sudden influx of marine water into the underfilled Permian basins of Europe (Smith, 1979) after a significant transgression occurred from the Barents Sea to the north (Strozyk et al., 2017). Both basins had restricted exchange of waters from the Northern Boreal Ocean and Southern Tethys Ocean (Pancost et al., 2002), leading to little influx of marine water. Despite the initial influx of large amounts of oceanic water, the sedimentation rate during this period remained low, which, combined with the high temperature, arid environment and limited water supplies, led to the Zechstein ocean becoming a giant evaporite production area in both of Europe's Permian basins (Glennie, 1998). This period of evaporite deposition occurred in the late Permian from 258 to 251 MA, according to chemical analysis of fluid inclusions found within Zechstein halite (Menning, 1995, Lippolt et al., 1993). The original depositional extent of the evaporite basin is represented by the modern-day distribution of the Zechstein (Jackson and Stewart, 2017).

The ZSGE's lithostratigraphy is separated into Zechstein cycles, commonly referred to as Z cycles, with either 5 or 7 in total, depending on the nomenclature used (Bailey et al., 1993, Geluk, 2007) (Figure. 2). The cycles' characterise cyclic evaporation and hence depositional sequences relating to periods of transgression and regression within the restricted basin (Pharaoh et al., 2010). Each depositional Zechstein cycle begins with lithologies associated with depositional environments in settings of low salinity, such as carbonates. As the progressive evaporation of the marine waters occurs, the salinity of the brine in the basin increases, and so do the subsequently deposited lithologies (Peryt et al., 2010). At the end of each Zechstein depositional cycle, evaporation of the brine will likely have occurred to total surface dryness until the next subsequent influx of water occurs (Glennie, 1998).

3. DATA

The study area (Figure. 3) is located within the South Permian Basin of the UKCS, a mature gas basin that has been explored and exploited for the last 50 years (Rouillard et al., 2020). The most western section is 20km offshore the east coast of England and extends east to the easternmost edge of the UK sector of the SNS. The most northern extent of the study area is defined by the Mid-North Sea high and stretches south 280km. All seismic and well data used in this study is available from the North Sea Transition Authority National Data Repository under an Open Government Licence.

3.1.1 Seismic data

The seismic data used in this study was the Southern North Sea Mega Survey Revision.2 (SNSMSR2) (Figure. 3), which was merged and processed by Petroleum Geo-Services (PGS) in 2015. This 3D merged seismic data set is comprised of 86 individual surveys from the UK sector of the SNS. The original datasets used in the merge were generally zero-phased 3D time-migrated seismic surveys. Each constituent survey was resampled to 4 ms, and inline/crossline grids interpolated to 12.5m if they were not already. Before the final merging process, to avoid miss-stacking, cleaning was done using a time-variant filter to reduce noise in deeper sections and a K-notch filter to clean up any jitter that had occurred in the shallow sections. Phase matching for the surveys within the merge was not undertaken. The merged survey covers a total area of 25,561 km^2. It has a line spacing of 12.5m, is zero phased and displayed using the European polarity standard, so that a negative amplitude represents an increase in impedance and a decrease in impedance is represented by a positive amplitude. The vertical resolution of the SNSMSR2 varies throughout the data set due to the constituent surveys having different original acquisition parameters, however, the vertical resolution varies between ~12m in the Cenozoic and ~52m in the Zechstein (Table 2.).

3.1.2 Well data

96 wells (Figure. 3) were used during this study. The wells that were used within this study were identified based on, but not limited to, if the well penetrated the ZSGE; the availability of petrophysical logs, specifically density, sonic, gamma rays and the availability of checkshot data. A full list of the wells used in this study can be found in Supplementary Table A.

3.2 METHODOLOGY

3.2.1 Well interpretation

Lithologies and stratigraphic boundaries were interpreted for the ZSGE (Figure. 4) using a combination of petrophysical properties, reference to lithology composite logs and cuttings descriptions. Lithologies for the ZSGE were defined for the minimum thickness interval possible using the petrophysical data, which, while dependent on the logging tool used, was between 0.3 and 2.5 m (Bourke et al., 1989). Lithologies for younger stratigraphy were also interpreted to enable a consistent stratigraphic framework to be constructed across the study.

Synthetic-seismic well ties were generated (Figure. 4) to correlate lithological and stratigraphic boundaries interpreted from wells to the seismic data. These well ties were generated using sonic and density logs, together with checkshot data. Synthetic traces generated using an analytical ricker wavelet and extracted wavelets were compared with the original seismic data to determine which wavelet was the best fit. In some cases, synthetic-seismic traces required time-shifting or stretching to account for mismatch in datums, largely a result of using a merged seismic volume. Figure 4 shows an example synthetic-seismic seismic trace overlaid on the coincident seismic trace from the NSMR 2 seismic data. The synthetic seismic traces generated frequently include high and low amplitude reflectors within the Zechstein interval that are not observed in the SNSMSR2 seismic volume (Figure. 4). These abnormally high and low synthetic seismic reflectors likely result from Z3 anhydrite being present within the well, which subsequently caused a high reflection coefficient and hence strong synthetic seismic reflector. Grant et al. (2019) also identify this issue and suggest that the anonymous high reflectors in the synthetic suggest that some areas of Z3 anhydrite within the Zechstein were not correctly imaged on seismic data due to the bed thickness being below the tuning thickness or in some instances steeply dipping.

3.2.2 Seismic interpretation

Major stratigraphic as well as lithological boundaries interpreted and identified from well data were subsequently interpreted in the 3D seismic, based on the seismic – well ties. Reflectors were initially mapped using an inline and crossline spacing of 100 and then auto-tracked and QC'd. Small isolated areas with low auto-tracking confidence were remapped at a reduced inline/crossline spacing, typically between 50 and 25 to improve the confidence in 3D auto-tracking. Surfaces were generated from the auto-tracked horizons to create seamless surfaces. A common problem with the SNSMSR2 survey is the lack of reflector continuity of the seabed reflector. This issue, also identified by Grant et al. (2019) is due to the shallow water depth of the North Sea. To counter this problem, instead of using a water bottom reflector, bathymetry data from EMODnet was used and converted to two-way travel time, assuming a water velocity of 1494 m/s, which is a similar approach to previous studies (e.g. Grant et al., 2019).

3.2.3 Structural facies interpretation

To interpret the internal deformation of the Zechstein evaporites, the internal reflection geometries were classified, principally constrained by the geometry of the prominent seismic reflectors of the Z3 Plattendolomit and the Z3 Hauptanhydrit (Figure. 4)

Based on these interpretations of the 3D seismic data, the structural facies were characterised based on the extent of interpreted deformation. The facies' interpretation included both inline and crosslines and from the geometries observed on interpreted surfaces in map view.

4. SEISMIC OBSERVATIONS AND RESULTS

The Zechstein Supergroup was the primary interval of focus. The base Zechstein is a prominent positive reflection across the area. Frequently small-scale extensional faults can be interpreted to displace the reflector (Figure. 5.A,B). The top Zechstein reflector is a negative reflection however since there is no significant velocity contrast (Figure. 4) between the overlying Triassic interval and the Zechstein, the event is generally a low amplitude reflection (Figure. 4). In areas of significant salt structuration, the steep dip can further exacerbate challenges in interpreting the top Zechstein. Within the Zechstein interval, the internal geometries vary significantly (Figure 5 - 10). In areas that are absent of major salt structures, the thickness of the ZSGE ranges from less than <47m (below seismic resolution) to >1.5km thick across the interpreted area (true vertical thickness) (Figure. 1). In areas of interpreted salt diapirs and walls, the thickness of the Zechstein can be >3km thick (true vertical thickness).

4.1 Structural facies characterisation

4.1.1 No resolvable deformation

Reflectors within the Zechstein are typically planar and laterally continuous (Figure 5.A) with a dip parallel to the underlying Z1 unit. All reflectors show a continuous reflection character (Figure 5.A) throughout the area. The seismic reflection amplitude of the Z2 is lower than those of the Z3 and Z4 (Figure 5.A). A uniform thickness change of 60ms can be identified within the Z2 towards the west of the cross-section (Figure. 5A), where seismic reflectors terminate. The overlying +Z3 also exhibits minor thickness changes, with a decrease in thickness towards the west, the same as observed in the Z2 (Figure 5.A). The Z4/5 has subtle thickness changes throughout between 12.5 - 20ms, however, these do not correlate with any underlying geology. The decrease of thickness in the Z3 correlates with the observed decreased thickness changes in the Z2 (Figure. 5.A). In these areas, the dip and dip direction change of reflectors are interpreted to relate to the dip of the underlying Rotliegend sediments rather than due to the influence or formation of salt-related structures. The average dip of the Z3 in this area is 2° with a maximum dip of 4°. There are no observed faults of folds within the salt in these areas.

The top Zechstein reflector normally has a planar geometry with little to no geometrical structure, if dip is occurring it is reflecting that of the regional geology, however, rare anticlines are present throughout these areas. Anticlines that are present within the top salt have large-scale wavelengths of 2.5 -10Km, with dip angles of limbs being <2°.

4.1.2 Minor internal deformation

The internal reflectors within the Zechstein are parallel to those of the base Zechstein, however, there are distinct areas where the reflectors display deformation in the form of a series of fold geometries (Figure. 6A). These fold geometries are observed to affect the +Z2 as well as the reflectors of the -Z3 (Figure. 6A). The folds have a wavelength of 1 – 3km an amplitude of 50 - 100ms and fold limbs which have dips ranging from 5 - 12°. The axial plane of the folds are typically inclined and asymmetrical, with each limb of the fold dipping differently. The traces of the fold axis are 1 – 5 km within this area and have no preferred orientation (Figure. 6C). Folds are not observed in the +Z3 and Z4/5 Zechstein units (Figure. 6).

The reflectors of the +Z3 and Z4/5 are continuous and can be traced extensively across the basin. The +Z3 and Z4/5 Zechstein cycles remain comparatively undisturbed by the deformation occurring in the Z2 and -Z3, the seismic reflectors, despite minor deformation above and the folds in the Z3, are parallel with one another and parallel with the top and base Zechstein reflectors. The interval from the top -Z3 reflector to the top Zechstein varies in thickness coincident with the fold patterns, with areas above synclines being up to 200m thicker than above the anticlines.

The base Zechstein Z1 has occasional extensional faults present trending NW – SE (Figure 6.A). These faults upward termination finishes at the top Z1 reflector, unaffecting the Z2 Zechstein, and terminates into the sub-Zechstein strata below, either the early Permian or Carboniferous sediments, with the Z1 being the main unit having been displaced. The faults have a throw ranging between 40 – 100ms, a heave between 50 – 200m.

Rare extensional faults are observed (Figure. 6.A) within the Z2 and -Z3, displacing the top of the Z2 and the base of the -Z3. The faults termination points are within the Z2 and -Z3. These faults have a length of 120 – 190 ms and a displacement of up to 95m.

The top salt within this area is commonly structured with anticlines and synclines. These have large wavelengths of 2.5 – 15km, an orientation of NW - SE. A large-scale gentle syncline can be seen in Figure 6. In areas where top salt is structured forming either anticlines or synclines, the -Z3 follows this trend, forming a large-scale fold with the top salt, following the geometry of the top Zechstein reflector, independent of the smaller folds present within the -Z3. While internally the ZSGE show evidence of significant deformation, the top of the interval remains relatively undeformed. As the deformation is entirely within the ZSGE, there is no observed deformation in the overlying Triassic, Cretaceous or Cenozoic.

4.1.3 Major internal deformation

The intra-Zechstein units exhibit prominent levels of deformation, having become further deformed, specifically within the Z2 and -Z3 units (Figure 2.). The seismic reflectors of the lower +Z2 are increasingly discontinuous and chaotic with asymmetrical fold structures being present (Figure 7.A), which are also present in the -Z3. The top +Z3 and Z4/5, by comparison, are still clear, continuous and have fewer structures (Figure. 7.A)

The fold geometries present in the Z2 and -Z3 have inclined axial planes and are asymmetrical with differing dips on each fold limb, similar to those seen in 4.1.2 (Figure. 7.A). The asymmetrical folds have a wavelength of 400m – 1km, amplitudes from 100 – 300ms and dip on the fold hinges typically ranging from 10 - 30°, with a max dip of 38. The fold traces of the structures range from 1500m – 9 Km in length (Figure 7.C). This area shows the fold axis trends in an NE – SW orientation, however, this has been observed to be different elsewhere within the basin, with axial trends also being N - S. Thickness changes are present within the +Z3 and Z4/5 units , these changes are coincident with the asymmetric peaks and troughs of the folds of the -Z3 and Z2 (Figure 7.A). Within the Z4 Zechstein units there are isolated reflectors which terminate onto the stratigraphically lower sections of Z4 (Fig 7.A.), which could be interpreted as onlap.

Occasional faults are present internally in the Zechstein, displacing the -Z3 and the top of the +Z2 within the Zechstein in this area (Figure 7.A). Normal and reverse faults (Figure 7.A) are observed, both of which terminate in the base Zechstein and the base of the +Z3. These faults have throws of ~40ms, a heave of ~80m, a length of ~200ms and a displacement of ~90 ms.

The base Zechstein Z1 continues to have been deformed by NW – SE trending extensional planar faults (Figure 7.A), however, they are more common and are larger than those observed in the minor deformation facies. The faults continue to terminate at the top Z1 reflector, with the top of the Z1 having been displaced into the Z2. The base termination for these faults is still pre-Zechstein strata however the length of these faults is observed to be greater than those present within in the minor deformation facies, being <1km in observable length on the seismic data. The faults now have a throw ranging between 40 – 120ms and a heave between 80 – 200m. The faults do not have any spatial relationship with the deformation occurring above within the Zechstein, as faults within the Z1 occur below both peaks, troughs and limbs of the folding in the above Z2 and -Z3.

The top Zechstein is commonly undeformed with no structure present, remaining parallel with the base Zechstein. However, similar observations to those in section 4.1.2 are seen here in the major area of internal deformation with some areas of the top Zechstein forming rare anticlinal and synclinal structures, which trend NW - SE. In Figure. 7.A the top Zechstein is forming a gentle syncline with a wavelength of 7.2km. The deformed -Z3, follows the top Zechstein's geometry to also form a gentle syncline of the same wavelength, independent of the asymmetric folds present in the -Z3.

4.1.4 Chaotic deformation

The Z2 unit is dominated by discontinuous seismic reflectors (Figure. 8.A). The individual reflectors within the Z2 can be differentiated with dips varying up to near vertical, they have orientations in parts that are unrelatable to any other reflectors within the Zechstein and in areas form broad fold geometries; however, it is challenging to differentiate any continuous structures within the data (Figure. 8.B).

The strong -Z3 seismic reflector, that was competent in the other previously identified structural facies, has ruptured, and broken apart into separate discreet sections of -Z3 (Figure. 8.A + 8.C), resulting in the mixing of the Z2 and Z3 salt units (Figure. 8). This breaking apart of Z3 has led to none-continuous sections of -Z3 being fully encased in the surrounding Z2 and +Z3 halite units, due to this the term rafts (Jackson and Hudec, 2017) has been applied. The rafts of -Z3 have varying geometries and orientations from horizontal to a dip of 70°. The area of these separate -Z3 rafts range from 0.02 to ~ 10km^2 (Figure. 8.C). The deformed rafts form a range of fold geometries with wavelengths of 1100 – 1600m, amplitudes of 65 – 195 ms and steeply dipping limbs on either side of with a max dip the same as the none-folded raft sections. No clear orientation can be seen within the trend line of the folds, with both symmetrical and asymmetrical folds being present. No spatial relationship between the differing -Z3 rafts can be observed (Figure 8.C). Rafts also overlap with one another (Figures. 8, A-C), possibly allowing minor connectivity between raft fragments once they have become separated.

The Z4/5 is not deformed to the same extent as the lower Zechstein units. The seismic reflectors remain parallel, with a constant thickness however the geometry of the Z4/5 unit as a whole has been greatly deformed as it now follows the geometry of the top Zechstein. No faulting is observed within the Z4/5 units. The continuity of the Z4/Z5 is only disturbed in areas where it has been pierced by the underlying Z2 and Z3 salt units.

The Z1 is now heavily faulted, with NW – SE trending extensional faults (Figure. 8.A). The faults are apparent every ~750m - ~3.5km, they have a greater displacement than previous Z1 extensional faults described in the minor/major deformation facies, with displacements of ~100 – 150 ms. The Z1 reflectors displace themselves significantly into the +Z2 above (Figure 8.A)

The top Zechstein is commonly deformed, forming anticlines and synclines with wavelengths of 3 – 15km and fold trend orientations of NW - SE. Some anticlines have ruptured, developing into areas in which the Z2/Z3 salt units are seen to pierce the overburden forming diapiric salt structures. The mobile salt that has intruded upwards into the overburden has thinned while doing so, becoming less clear on seismic data. The sections where the overburden has been pierced occurs at the hinge of anticlines in the top Zechstein, or in areas where faults within the overburden come into contact with the top Zechstein. The intruding salt protrudes 90 – 600ms and follows the orientation of the anticlines original axial plane or the fault.

4.1.5 Area of withdrawal

These areas are exclusively found adjacent to major salt structures, such as salt walls and diapirs. This includes surrounding the large salt anticlines. These facies form predominantly elongate oval-shaped areas that align with the salt structures they flank, for example, the middle basin salt walls are completely encased by this facies, also trending WNW – ESE.

The Z2, is thinner than elsewhere in the basin, being >42-47 m thick. In some sections (Figure 9.A) the lack of Z2 halite is such that the Z5 and Z1 could be interpreted as being in contact with one another, forming an intra-Zechstein salt weld. The visible patches of Z2 salt have planar seismic reflectors present within. Small areas of high amplitude reflectors are present in the remnants of the Z2 salt (Figure. 9.A). The Z3 unit is not visible, unlike the other structural facies observed within the basin(Figure. 9.A). The isolated high amplitude patches present within these areas may be remnants of the -Z3 having undergone brittle deformation.

Post-Zechstein strata is thickened above these deformation areas, especially within the Cenozoic sedimentary deposits (Figure 2.). The fringes of these facies always show dips pointing towards the lowest point of top salt, forming large-scale synclines ranging from 100m - 10's kms scale.

4.1.6 Undifferentiated deformation

Seismic reflectors are not coherent for any section of the Zechstein (Figure. 10.A), rather the seismic data for these facies portrays the structure as one large crystalline mass. The lithostratigraphy within these areas can no longer be interpreted as it could in the other internal structural facies. These structural facies typically coincide with salt structures, such as salt walls, diapirs or large anticlines and are trending NW - SE. The flanks of these areas are typically surrounded by the withdrawal deformation facies (figure 10.A).

In rare areas, sections, small packages of nonchaotic, high reflection amplitude material are visible (figure 10.A); these small packages are only visible on seismic for less than 1 km and have low dips. Wells used within this study that have drilled through these facies, show more heterogeneity than is present in the seismic data. Interbeds of greater than the seismic resolution are present but have not been imaged correctly.

4.2 Map view of internal Zechstein structural facies

The spatial distribution of the different internal structural facies of Zechstein deformation is shown in Figure. 11. The distinct structural facies commonly coincide with facies of the adjacent levels of deformation; however, areas of undifferentiated salt do appear enclosed within all structural facies that have been identified.

5. DISCUSSION

5.1 Variation in structural styles

The structural facies identified provides evidence of spatially varying strain within the ZSGE (Figures. 5-7). The distribution of the 6 identified structural facies can be broadly split into 3 distinct structural domains (Figure. 11). Domain A, which is located in the proximal area of the basin, is characterised by the no deformation and the minor deformation facies. Small areas of undifferentiable structural facies are present sporadically throughout this domain. Domain B, within the central region of the study area, is dominated by the withdrawal and undifferentiable facies, trending NW – SE. This domain is characterised by large salt structures, including areas of salt expulsion which have fed these structures. Finally, domain C is located in the most distal part of the basin and is dominated by the chaotic structural facies. Domain C is the most diverse of the observed domains, with every characterised structural facies being present within it. A general trend derived from the spatial distribution of structural facies and hence domains is the increasing levels of internal deformation from proximal areas of the basin towards the distal areas of the basin, with a breach of salt structures in the transitional areas of the basin.

Salt does not flow spontaneously, instead, it reacts to external changes in stress (Jackson and Stewart, 2017); this applies to the formation of both major salt structures, i.e. diapirs, and the internal structures described in this study. The dominant force involved with salt flow is recognised as differential loading, either gravitational, thermal, or displacement (Hudec and Jackson, 2007). In this study the intensity of internal deformation is observed to increase basinward (Figure. 11), suggesting that gravity is the dominant force for internal deformation. The magnitude of shortening increases basinward, as evidenced by the changes in observed fold structures (Figures. 6,7) towards the basin depocenter. Observed areas of folding within the -Z3 which have specific orientations that align with salt flow towards the basin centre (Figure 7.C) supports the interpretation that gravitational gliding is the most likely mechanism to have formed the main intra-Zechstein structural deformation.

Two consistent observations for the characterised internal structural facies of the Zechstein are; 1) the vertically varying levels of deformation, in that each Z cycle at a set vertical point has undergone a different amount of strain; The vertical stratification and partitioning of deformation is likely a result of two separate factors, lithology and hence rheology, as different lithologies have different rheology's (Burliga, 1996) and types of flow present and occurring internally within the Zechstein (Davison et al., 1996); and 2). The undeformed overburden in areas of intense internal deformation. This is likely a result of shear between the top salt and overburden (Cartwright et al., 2012), leading to the top salt being mechanically decoupled from the overburden (Evans and Jackson, 2021).

Figures 2 and 4 show that the Zechstein supergroup is highly heterogenous, comprised of 4 main different lithologies repeating in the Zechstein 1-5 cycles (Figure. 2). These cycles and changes in lithology lead to a rheological stratification (Rowan et al., 2019) which is often seen in LES, and is present within the Zechstein (Figure 12. E, F). This rheological stratification and hence mechanical stratigraphy affects how intra-salt units accommodate strains and stresses applied to them (Evans and Jackson, 2021). These parameters control the structural styles that develop within LES. It has been observed within LES with low competency contrasts between lithologies that low amplitude cuspate-lobate folds develop, however, in LES with high competency contrasts, such as within our study area, high amplitude buckle folds develop (Rowan et al., 2019) like those observed in Figures, 6-8.

5.2 Flow regimes

The observed internal deformation of the Zechstein (Figure. 5 – 8) is likely indicative of the salt's dominant flow regime (Figure. 12 A - D). Nearly all flows occurring within salt units are hybrids, however, comparing to ideal flows provides a good base point for identifying the type of flow occurring (Jackson and Hudec, 2017). The observations made in the study area suggest that the stratigraphic middle of the Zechstein, where the -Z3 is located, has experienced the highest magnitudes of longitudinal strain (Figure 12. A,C,E,F), with lower magnitudes occurring stratigraphically below and above. While in some cases line reconstruction can be used to further evaluate the likely dominant flow within a hybrid flow system (e.g. Cartwright et al., 2012), the structures in the Z2 are poorly resolved and therefore the geometries are uncertain. The structures that are resolved in the +Z2 indicate a higher strain rate at the base of the Zechstein compared with the Z3+, Z4/5 (Figures 5 – 9), which is unusual for typical flow deformation styles (Figure. 12). The +Z2 commonly has asymmetrical folds (Figures. 6,7,8) present and deformed seismic reflectors directly below the Z3+, Z4/5 reflectors which are undeformed. The observed geometries of the LES shown could be explained by a number of possible different flow profiles are;

1) Simple Couette flow (Simple Shear) (Figure. 12 B and E) of the Z2 and Z3- with the Z3+/4/5 acting as the overburden and the Z1 acting as the underburden. Observations to support this

possible flow profile include the increasing strain from the Z2 into the -Z3, the lack of any strong deformation, with seismic reflectors remaining parallel to one another in the Z3+/4/5 and no deformation in the Z1. This flow profile would also explain the geometry that Z4/5 take in Figure. 8, where it has been uniformly deformed with/and is behaving like the overburden.

2) Asymmetric Poiseuille flow (Figure 12. C and F) could also be a possible alternate dominant flow profile. If this is the dominant profile, no intra-Zechstein shear zones exist. Observations that aid this possibility are maximum strain being constrained to the middle -Z3 unit, with it allowing for asymmetric levels of deformation stratigraphically, with greater levels of deformation occurring in the Z2 over the Z3+/4. In this flow profile, the Z1 is still behaving as a detachment layer for the Zechstein, and the upper Z4/5 is behaving like the overburden.

Additionally, the larger extent of the LES may also affect the dominant flow profile, as described by Rowan et al. (2019) in the Levant basin, where it is interpreted that flow initiated with Couette flow being dominant, but as external geometries of the salt evolve so does the shear profile, for example, shear being increasingly localised under synclines. These observations from the Levant basin could aid in part with understanding features seen within areas of the SPB, such as the Chaotic structural facies; where the stratigraphically partitioned levels of increased strain in lower Z3/Z2 Zechstein are present compared with the stratigraphically higher Z4/5 Zechstein in externally structured areas (Figure. 8) and higher levels of complex salt deformation that occur within anticline cores.

Having identified these structural facies, we can hypothesise the pathways for internal deformation that the Zechstein underwent. Prior to gravitational loading leading to the Zechstein being subjected to shear, there is no deformation, with no external or internal structures evident. The structural facies characterised within the study area, minor, major and chaotic structural, indicate a progressive increase in strain. The minor and major facies have undergone ductile compressional deformation internally, with the only difference being the magnitude of compression occurring, the minor deformation facies being a precursor salt deformation stage to the major deformation facies.

The minor, major and chaotic facies have experienced compressional stresses, as seen by the folded features observed in each facies (Figures. 6 – 9). These internal compressional folds often occur; without affecting the overburden, with a lack of structure to the top salt, without compressional faults in the Zechstein or overburden and no syn-kinematic thinning strata above these areas. The lack of such apparent compressional features below or above the Zechstein suggests that much of this compression may have been restricted to solely within the Zechstein. The trend of the structural facies and the distribution of these suggests a lateral distribution of the compressional stress increasing with distance down dip. Increasing stress down-dip within the Zechstein is likely the result of gravitational loading from the slope dip of the pre-salt (Figure 1.) and Basin tilt (Stewart and Coward, 1995). To add to this extensional features are observed up-dip at the fringes and just outside our area of research (Figure 1.), a feature which is an expected component of a gravity gliding system (M. Pichel et al., 2019). These observations combined with the identified features or lack thereof, rule out other mechanisms as the most likely driving force behind the observed internal structural facies of the Zechstein, mechanisms such as displacement loading or thermal loading, and hence gravitational loading and gravity gliding is the most obvious explanation.

5.3 Chaotic facies

The chaotic facies demonstrates a continuation in the increased magnitude of compressional deformation (Figure. 8) observed throughout the structural facies within the research area. However, the presence of discontinuous rafts leaves questions about both timing and origin.

Rafts have been observed through many different LES (Archer et al., 2012) and have been recognised and described in the Zechstein previously (Van Gent et al., 2011). Boudinage is a common feature of competent layers, such as anhydrites and carbonates, that are enclosed within a weak, ductile matrix, such as halite, and undergo layer-parrel extension (Rowan et al., 2019), as generally competent rocks are more likely to undergo brittle failure in extension than compression. This mechanism of boudinage via extension for raft formation is suggested by Strozyk et al. (2014) for the formation of the -Z3 rafts in the Dutch sector of the SNS. However, within our research area there are observations that suggest boudinage is not the correct mechanism for raft formation; 1). areas of pure boudinage internally within the Zechstein are not observed, expected observations for such an area would be discontinuous segments of planar -Z3 rafts with no folding structures of any type and perhaps layer parallel extension; 2). Areas of the chaotic deformation facies exist without extensional strata packages in the overburden and little to no deformation to the top Zechstein. However, it is worth nothing that this second point is countered if, as 2014 suggests, the boudinage occurred before the deposition of any stratigraphy above the Zechstein.

We suggest an alternate mechanism for the formation of the rafts observed within the Zechstein of the SNS. From our observations, the formation of the rafts must have occurred after the formation of the compressional folds as to allow the rafts to inherit the geometry of the compressional folds. Further to this, with the severity of deformation increasing from the major deformation facies to the chaotic, the levels of dip observed within fold limbs have increased as the rotation from salt flow has continued. Formation of the rafts by brittle failure of the -Z3 during compression from the salt flow is a likely origin of these discontinues features. This mechanism for the raft formation then allows for the correct timing (after the intense level of folding), the severe compressional geometries observed and the apparent lack of any extensional features within this area of the Zechstein and basin.

Further to this, with the increased magnitude of compressional deformation geometries occurring in the chaotic structural facies, the appearance of features that may be interpreted as rafts on seismic may be explained as parts of the -Z3 where the dip is too great to be resolved correctly by the seismic data. While we are not suggesting a complete lack of rafts, as evident from the well data, it would explain observations on our seismic data. For example, small isolated high amplitude reflectors being present between two higher-up rafts on either side likely represents a fold hinge in between two near vertical fold limbs. Figure. 8 has been interpreted to show these possible unresolvable areas of -Z3.

5.4 Withdrawal and undifferentiable facies

The withdrawal structural facies reflect areas where salt has flowed away from the deposited area. Observed within these facies are areas with and without high amplitude reflectors present internally (Figure. 9). The main high amplitude reflectors internally within the Zechstein are composed of the Z3 and rafts of Z3 (Figure 6, - 9), the most obvious suggestion for the origin of these high amplitude packages is that they are remanent -Z3 rafts which have not flowed with the more mobile lithologies into surrounding salt structures. Areas of withdrawal with high amplitude patches are often located next to chaotic structural facies. If the rafts formed from boudinage of the brittle -Z3 due to syn-depositional gravity gliding, as suggested in earlier paragraphs, the rafts predate the timing of withdrawal and would be present during the mobilisation to feed the surrounding salt structures; hence rafts could have been mobilised by the salt flow and be present in structures or left as remnant rafts in these intra-Zechstein salt welds (Figure. 9B). This suggests we can identify what residual components that may remain within the specific areas of withdrawal facies by observing the surrounding structural facies, e.g. withdrawal facies located next to major deformation facies is unlikely to have any remnant rafts in and hence surrounding structures won't, whereas those located next to chaotic facies are likely to have them present. These possibilities have valuable implications for LES with poorly imaged seismic data, as they may allow for an idea of what internal heterogeneities may be present in areas of salt withdrawal that have been poorly imaged.

Due to the nature of the undifferentiable facies being a product of the inability of the seismic data to image the internals of salt, rather than the structural heterogeneity present within the salt itself, it is difficult to determine where exactly areas within these facies fit into the deformation pathway. The use of analogues may be helpful to determine the exact internal structure the undifferentiable areas within the study area may have taken. The best analogues of the internal structure of diapirs originate from mined evaporite structures that have been mapped, with those such as the Hanigsen – Wathlingen salt dome, which shows boudinaged and incoherent Z cycles within the salt (Pichat, 2022), or the Bartensleben Diapir, where the internal Zechstein units are deformed but still competent and distinguishable (Pichat, 2022). Identifying the surrounding dominant structural facies of salt bodies, be that the none, minor, major, or chaotic deformation facies, could be indicative of the internal geometries and heterogeneities that occur internally within the salt structures, much like what was observed in the withdrawal facies with remnant high amplitude reflectors, which, were interpreted to be Z3 rafts (Figure 9, 13). However, without better-imaged salt structures, it is impossible to tell what the true internal structural heterogeneity of these structures is.

6. CONCLUSIONS

The Zechstein of the South Permian Basin can be characterised by 6 distinct internal structural facies. Each facies represents a distinct type of internal deformation or unique salt deformation. These internal structural facies of the Zechstein can be further grouped into 3 distinct broader domains throughout the basin. Observations indicate that a combination of the type of internal salt flow and the variation in vertical mechanical stratigraphy control the structural facies and the internal geometries that form within the Zechstein.

Isolated high amplitude seismic reflectors present within areas of salt expulsion, such as salt welds, can be identified due to the surrounding internal structural facies of the LES, which reduces uncertainty in areas with poor seismic or bad well control data available.

The internal geometries that form within an LES are recognised to be an important geological feature to characterise and hence reduce uncertainties in the characterisation of geo-storage projects. Not fully understanding the internal complexities LES possess may prove costly and time-consuming to remedy at best for geo-storage projects, or could cause loss of the project altogether at worst if they are not carefully understood.

Vii. REFERENCES

AAL, A. A., EL BARKOOKY, A., GERRITS, M., MEYER, H., SCHWANDER, M. & ZAKI, H. 2000. Tectonic evolution of the Eastern Mediterranean Basin and its significance for hydrocarbon prospectivity in the ultradeepwater of the Nile Delta. *The Leading Edge,* 19**,** 1086-1102.

ADAMUSZEK, M., TĂMAŞ, D. M., BARABASCH, J. & URAI, J. L. 2021. Rheological stratification in impure rock salt during long-term creep: morphology, microstructure, and numerical models of multilayer folds in the Ocnele Mari salt mine, Romania. *Solid Earth,* 12**,** 2041-2065.

ARCHER, S. G., ALSOP, G. I., HARTLEY, A. J., GRANT, N. T. & HODGKINSON, R. 2012. Salt tectonics, sediments and prospectivity: an introduction. *Geological Society, London, Special Publications,* 363**,** 1-6.

BAILEY, J. B., ARBIN, P., DAFFINOTI, O., GIBSON, P. & RITCHIE, J. S. 1993. Permo-Carboniferous Plays of the Silver Pit Basin. *Petroleum Geology of Northwest Europe: Proceedings of the 4th Conference***,** 707-715.

BOURKE, L., DELFINER, P., FELT, T., GRACE, M., LUTHI, S., SERRA, O. & STANDEN, E. 1989. Using formation Microscanner images: The (Schlumberger) Technical Review.

BURLIGA, S. 1996. Kinematics within the Kłodawa salt diapir, central Poland. *Geological Society, London, Special Publications,* 100**,** 11-21.

BUTLER, R. W. H., MANISCALCO, R., STURIALE, G. & GRASSO, M. 2015. Stratigraphic variations control deformation patterns in evaporite basins: Messinian examples, onshore and offshore Sicily (Italy). *Journal of the Geological Society,* 172**,** 113-124.

CAGLAYAN, D. G., WEBER, N., HEINRICHS, H. U., LINßEN, J., ROBINIUS, M., KUKLA, P. A. & STOLTEN, D. 2020. Technical potential of salt caverns for hydrogen storage in Europe. *International Journal of Hydrogen Energy,* 45**,** 6793-6805.

CARTWRIGHT, J., JACKSON, M., DOOLEY, T. & HIGGINS, S. 2012. Strain partitioning in gravity-driven shortening of a thick, multilayered evaporite sequence. *Geological Society, London, Special Publications,* 363**,** 449-470.

CARTWRIGHT, J., STEWART, S. & CLARK, J. 2001. Salt dissolution and salt-related deformation of the Forth Approaches Basin, UK North Sea. *Marine and Petroleum Geology,* 18**,** 757-778.

CLARK, J. A., STEWART, S. A. & CARTWRIGHT, J. A. 1998. Evolution of the NW margin of the North Permian Basin, UK North Sea. *Journal of the Geological Society,* 155**,** 663-676.

DAVISON, I., ALSOP, I. & BLUNDELL, D. 1996. Salt tectonics: some aspects of deformation mechanics. *Geological Society, London, Special Publications,* 100**,** 1-10.

ERRATT, D., THOMAS, G. M. & WALL, G. R. T. 1999. The evolution of the Central North Sea Rift. *Geological Society, London, Petroleum Geology Conference series,* 5**,** 63-82.

EVANS, S. L. & JACKSON, C. A. L. 2021. Intra-salt structure and strain partitioning in layered evaporites: implications for drilling through Messinian salt in the eastern Mediterranean. *Petroleum Geoscience,* 27.

GELUK, M. 2007. Permian *In:* WONG, BATJES & JAGER, D. (eds.) *Geology of the Netherlands.* Royal Netherlands Academy of Arts and Sciences.

GLENNIE, HIGHAM & STEMMERIK 2003. Chaper 8 Permian. *In:* EVANS, D., GRAHAM, C., ARMOUR, A. & BATHURST, P. (eds.) *The Millenium Atlas.* The Geological Society of London.

GLENNIE, K. W. 1998. *Petroleum Geology of the North Sea: Basic Concepts and Recent Advances*, Blackwell Scoence.

GLENNIE, K. W. & UNDERHILL, J. R. 1998. Origin, Development and Evolution of Structural Styles. *Petroleum Geology of the North Sea.*

GRANT, R. J., UNDERHILL, J. R., HERNÁNDEZ-CASADO, J., BARKER, S. M. & JAMIESON, R. J. 2019. Upper Permian Zechstein Supergroup carbonate-evaporite platform palaeomorphology in the UK Southern North Sea. *Marine and Petroleum Geology,* 100**,** 484-518.

GUDMUNDSSON, A. 2012. *Rock Fractures in Geological Processes*.

HANAFI, B. R., WITHJACK, M. O., DURCANIN, M. A. & SCHLISCHE, R. W. 2022. The development of the eastern Orpheus rift basin, offshore eastern Canada: A case study of the interplay between rift-related faulting and salt deposition and flow. *Marine and Petroleum Geology,* 139.

HODGSON, N. A., FARNSWORTH, J. & FRASER, A. J. 1992. Salt-related tectonics, sedimentation and hydrocarbon plays in the Central Graben, North Sea, UKCS. *Geological Society, London, Special Publications,* 67**,** 31-63.

HUDEC, M. R. & JACKSON, M. P. A. 2007. Terra infirma: Understanding salt tectonics. *Earth-Science Reviews,* 82**,** 1-28.

JACKSON, C. A. L., JACKSON, M. P. A., HUDEC, M. R. & RODRIGUEZ, C. R. 2015. Enigmatic structures within salt walls of the Santos Basin—Part 1: Geometry and kinematics from 3D seismic reflection and well data. *Journal of Structural Geology,* 75**,** 135-162.

JACKSON, C. A. L. & STEWART, S. A. 2017. Composition, Tectonics, and Hydrocarbon Significance of Zechstein Supergroup Salt on the United Kingdom and Norwegian Continental Shelves: A Review. *In:* SOTO, FLINCH & TARI (eds.) *Permo-Triassic Salt Provinces of Europe, North Africa and the Atlantic Margins.* Elsevier.

JACKSON, M. P. A. & HUDEC, M. R. 2017. *Salt Tectonics*, Cambridge University Press.

JOHNSON, WARRINGTON & STOKER 1993. *Lithostratigraphic Nomenclature of the UK North Sea: Permian and Triassic of the Southern North Sea v. 6*, British Geological Survey.

JONES, I. F. & DAVISON, I. 2014. Seismic imaging in and around salt bodies. *Interpretation,* 2**,** SL1-SL20.

KERNEN, R., LEHRMANN, A. & PIPER, P. 2021. Lithostratigraphy and chemostratigraphy of salt diapir sedimentary inclusions: unravelling Ediacaran salt–sediment interaction in the Flinders Ranges. *MESA Journal,* 95**,** 4 - 29.

KIRKHAM, C. & CARTWRIGHT, J. 2021. Restoration of multiphase salt tectonic deformation using passive strain markers. *Basin Research,* 33**,** 2453-2473.

LIPPOLT, HAUTMANN & PILOT 1993. 40 Ar/39 Ar-Dating of Zechstein Potash Salts: New Constraints on the Numerical Age of the Latest Permian and the P-Tr Boundary. *EUG (European Union of Geosciences) VII, Terra Abstract.*

LUANGTHIP, A., WILALAK, N., THONGPRAPHA, T. & FUENKAJORN, K. 2017. Effects of carnallite content on mechanical properties of Maha Sarakham rock salt. *Arabian Journal of Geosciences,* 10.

LUX, K. H. 2009. Design of salt caverns for the storage of natural gas, crude oil and compressed air: Geomechanical aspects of construction, operation and abandonment. *Geological Society, London, Special Publications,* 313**,** 93-128.

M. PICHEL, L., FINCH, E. & GAWTHORPE, R. L. 2019. The Impact of Pre-Salt Rift Topography on Salt Tectonics: A Discrete-Element Modeling Approach. *Tectonics,* 38**,** 1466-1488.

MAYNARD, J. R. & GIBSON, J. P. 2001. Potential for subtle traps in the Permian Rotliegend of the UK Southern North Sea. *Petroleum Geoscience,* 7**,** 301-314.

MENNING, M. 1995. A Numerical Time Scale for the Permian and Triassic Periods: An Integrated Time Analysis. *The Permian of Northern Pangea.*

MIOCIC, J. M., JOHNSON, G. & GILFILLAN, S. M. V. 2014. Fault seal analysis of a natural CO2 reservoir in the Southern North Sea. *Energy Procedia,* 63**,** 3364-3370.

PANCOST, R. D., CRAWFORD, N. & MAXWELL, J. R. 2002. Molecular evidence for basin-scale photic zone euxinia in the Permian Zechstein Sea. *Chemical Geology,* 188**,** 217-227.

PATRUNO, S., KOMBRINK, H. & ARCHER, S. G. 2022. Cross-border stratigraphy of the Northern, Central and Southern North Sea: a comparative tectono-stratigraphic megasequence synthesis. *Geological Society, London, Special Publications,* 494**,** 13-83.

PERYT, T., GELUK, M., MATHIESEN, M., PAUL, J. & SMITH, K. 2010. Chapter 8 Zechstein. *In:* DOORNENBAL, H. & STEVENSON, A. (eds.) *Petroleum Geological Atlas of the South Permian Basin Area.*

PHARAOH, T., DUSAR, M., GELUK, M., KOCKEL, F., KRAWCZYK, C., KRZYWIEC, P., SCHECK-WENDEROTH, M., THYBO, H., VEJBAEK, O. & VAN WEES, J. 2010. Chapter 3: Tectonic Evolution.

PICHAT, A. 2022. Stratigraphy, Paleogeography and Depositional Setting of the K–Mg Salts in the Zechstein Group of Netherlands—Implications for the Development of Salt Caverns. *Minerals,* 12.

ROUILLARD, P., BAGLEY, G., MOSELEY, D., MYERS, K. & HARDING, A. 2020. UKCS exploration: 50 years and counting. *Geological Society, London, Memoirs,* 52**,** 32-42.

ROWAN, M. G., URAI, J. L., FIDUK, J. C. & KUKLA, P. A. 2019. Deformation of intrasalt competent layers in different modes of salt tectonics. *Solid Earth,* 10**,** 987-1013.
SARG, J. F. 2001. The sequence stratigraphy, sedimentology, and economic importance of evaporite–carbonate transitions: a review. *Sedimentary Geology,* 140**,** 9-34.
SCHULMANN, K., CATALÁN, J. R. M., LARDEAUX, J. M., JANOUŠEK, V. & OGGIANO, G. 2014. The Variscan orogeny: extent, timescale and the formation of the European crust. *Geological Society, London, Special Publications,* 405**,** 1-6.
SMITH, D. B. 1979. Rapid marine transgressions and regressions of the Upper Permian Zechstein Sea. *Journal of the Geological Society,* 136**,** 155-156.
STEWART, S. A. & COWARD, M. P. 1995. Synthesis of salt tectonics in the southern North Sea, UK. *Marine and Petroleum Geology,* 12**,** 457-475.
STROZYK, F., REUNING, L., SCHWECK-WENDEROTH, M. & TANNER, D. C. 2017. Chapter 10 - The Tectonic History of the Zechstein Basin in the Netherlands and Germany. *In:* SOTO, J., FLINCH, J. F. & TARI, G. (eds.) *Permo-Triassic Salt Provinces of Europe, North Africa and the Atlantic Margins.* Elsevier.
STROZYK, F., URAI, J. L., VAN GENT, H., DE KEIJZER, M. & KUKLA, P. A. 2014. Regional variations in the structure of the Permian Zechstein 3 intrasalt stringer in the northern Netherlands: 3D seismic interpretation and implications for salt tectonic evolution. *Interpretation,* 2**,** SM101-SM117.
TARKOWSKI, R. & CZAPOWSKI, G. 2018. Salt domes in Poland – Potential sites for hydrogen storage in caverns. *International Journal of Hydrogen Energy,* 43**,** 21414-21427.
THOMAS, D. W. & COWARD, M. P. 1996. Mesozoic regional tectonics and South Viking Graben formation: evidence for localized thin-skinned detachments during rift development and inversion. *Marine and Petroleum Geology,* 13**,** 149-177.
VAN DALFSEN, W., DOORNENBAL, J. C., DORTLAND, S. & GUNNINK, J. L. 2016. A comprehensive seismic velocity model for the Netherlands based on lithostratigraphic layers. *Netherlands Journal of Geosciences - Geologie en Mijnbouw,* 85**,** 277-292.
VAN GENT, H., URAI, J. L. & DE KEIJZER, M. 2011. The internal geometry of salt structures – A first look using 3D seismic data from the Zechstein of the Netherlands. *Journal of Structural Geology,* 33**,** 292-311.
WEIMER, P., BOUROULLEC, R., ADSON, J. & COSSEY, S. P. J. 2017. An overview of the petroleum systems of the northern deep-water Gulf of Mexico. *AAPG Bulletin,* 101**,** 941-993.
WEN, Z., JIANG, S., SONG, C., WANG, Z. & HE, Z. 2019. Basin evolution, configuration styles, and hydrocarbon accumulation of the South Atlantic conjugate margins. *Energy Exploration & Exploitation,* 37**,** 992-1008.
WONG, T. E., DE LUGT, I. R., KUHLMANN, G. & OVEREEM, I. 2007. Tertiary. *In:* WONG, BATJES & JAGER, D. (eds.) *Geology of the Netherlands.* Royal Netherlands Academy of Arts and Sciences.
ZANELLA, E. & COWARD, M. P. 2003. Chapter 4 Structural Framework. *The Millennium Atlas: petroleum geology of the central and northern North Sea.* The Geological Society of London.
ZIEGLER, P. A. 1990. *Geological Atlas of Central and Western Europe*, The Hague : Shell International Petroleum Maatschappij B.V.
ZULAUF, J. & ZULAUF, G. 2005. Coeval folding and boudinage in four dimensions. *Journal of Structural Geology,* 27**,** 1061-1068.
ZULAUF, J., ZULAUF, G., HAMMER, J. & ZANELLA, F. 2011. Tablet boudinage of an anhydrite layer in rock-salt matrix: Results from thermomechanical experiments. *Journal of Structural Geology,* 33**,** 1801-1815.

Viii. Tables

Lithology	Compressive Strength (MPa)	Tensile Strength (MPa)
Anhydrite	70 – 120	5 – 12
Carbonate - Dolomite	80 – 250	3 – 25
Carbonate - Limestone	4 – 250	1 – 25
Halite	24	2
carnallite	10	0.5

Table 1. Lithologies present within layered evaporite sequences. Anhydrite and Carbonate values from Gudmundsson (2012), Halite Values from Jackson and Hudec (2017) and Carnallite values from Luangthip et al. (2017)

Main Unit	Depth (ms)	Dominant Frequency (Hz)	Seismic Velocity (m/s)	Vertical Seismic Resolution (m) λ = ((Hz / m/s)/4)	Notes
Cenozoic	-110 to -900	45	1872	12	Velocity extracted from wells in this study
Cenozoic	-110 to -900	40	1777	11	Velocity from (van Dalfsen et al., 2016)
Cretaceous, Jurassic, Triassic	-900 to -1700	35	3186	18.2	Average Velocity extracted from wells
Cretaceous, Jurassic, Triassic	-900 to -1700	35	2548	32	Average Velocity from (van Dalfsen et al., 2016)
Zechstein	-1700 to -2300	26.5	4500	42	Zechstein Low Seismic Velocity (van Dalfsen et al., 2016)
Zechstein	-1700 to -2300	26.5	5500	51	Zechstein High Seismic Velocity. (van Dalfsen et al., 2016)

Table 2. Seismic resolution examples for slice Inline 31000 – 35000, Crossline 32000 – 35000 from the SNSMSR2 . Resolutions have been calculated for specific Time values. Velocities used were both extracted from wells and taken from literature, as denoted in the table.

ix. Figure Legends/Captions

Figure 1. An WSW-ENE trending regional cross-section of the South Permian Basin from onshore UK to the edge of the UKCS. The main structural elements and stratigraphy (Quaternary - Pre-Permian) within the South Permian Basin are visible. Redrawn from Pharaoh et al. (2010). The map view of the cross-section can be seen in Figure. 3 as A – A'. Important geographical areas within the South Permian Basin have also been labelled.

Figure 2. Chronostratigraphic chart of the stratigraphy of the Southern Permian Basin running N – S through the basin centre modified from, Patruno et al. (2022). All major stratigraphic successions are shown, as well as unconformities. The Lithostratigraphy of the Zechstein Supergroup, alongside the consistent Zechstein cycles, are included. The nomenclature for the Zechstein is from Johnson et al. (1993), with all Zechstein cycles and comprising lithologies present. MMU = Mid Miocene Unconformity, AU = Atlantean Unconformity, BCU = Base Cretaceous Unconformity, SP Fm = Silverpit Formation, Rtlgd = Rotliegend, MNSH = Mid North Sea High, BPU = Base Permian Unconformity

Figure 3. Location and data map for UKCS SNS. Summary overview of all data used within this study and its geographical location. The top left map shows the study location with respect to the UK and Europe. The Southern North Sea Mega Survey Revision.2 (blue) seismic survey outline is present, alongside well data use within this paper. Locations of all present well data within the Southern North Sea are also marked on the map.

Figure 4. Petrophysical logs, interpreted lithology log and synthetic-seismic well ties of Well 44/27-2 in the SNS. 44/27-2 is located within the depocenter of the SNS basin, and its geospatial position can be seen as marked in Figure. 3 Petrophysical logs shown are Sonic (DT) and Density (RHOB). An interpreted lithology log is also present as well as interpreted formations and Zechstein cycles. Lithological interpenetration for the Zechstein was undertaken at the same resolution as the petrophysical logs allowed; interpretation of none Zechstein formations occurred at a lower resolution, such that only major formation changes were noted.

Figure 5. A Seismic section (B – B') of the Zechstein from the SNSMSR2, (A) uninterpreted and (B) interpreted running W – E in an area characterised as unresolvable deformation. The vertical axis is in two–way travel time. See Figure 11 for location. Important reflectors have been marked on the right-hand side of both A and B, TZ (Top Zechstein), TZ3 (Top Z3), TZ2 (Top Z2), TZ1 (Top Z1) and BZ (Base Zechstein). (C) Dip surface of the Z3 reflector of this cross-section in a plane view, with the location of the cross-section marked in red.

Figure 6. A Seismic section (C – C') of the Zechstein from the SNSMSR2, (A) uninterpreted and (B) interpreted running SW – NE in an area characterised as minor internal deformation. The vertical axis is in two–way travel time. See Figure 11 for location. Important reflectors have been marked on the right-hand side of both A and B, TZ (Top Zechstein), TZ3 (Top Z3), TZ2 (Top Z2), TZ1 (Top Z1) and BZ (Base Zechstein). (C) Dip surface of the Z3 reflector of this cross-section in a plane view, with the location of the cross-section marked on in red. Figure.6 C,

shows the surface view of the Z3 and the geometries in 3D space these asymmetrical folds take.

<u>Figure 7.</u> A Seismic section (D – D') of the Zechstein from the SNSMSR2, (A) uninterpreted and (B) interpreted running SW – NE in an area characterised as major internal deformation. The vertical axis is in two–way travel time. See Figure 11 for location. Important reflectors have been marked on the right-hand side of both A and B, TZ (Top Zechstein), TZ3 (Top Z3), TZ2 (Top Z2), TZ1 (Top Z1) and BZ (Base Zechstein). (C) TWT depth surface (ms) of the Z3 reflector within the major deformation facies. The axial trends of the folds present have been marked on in yellow. (D) Dip surface of the Z3 reflector of this cross-section in a plane view, with the location of the cross-section marked in red. (E) A Dip surface map of the Z1 Zechstein unit, demonstrating the faults present within the base Zechstein, the faults have been marked with a green line.

<u>Figure 8.</u> A Seismic section (E – E') of the Zechstein from the SNSMSR2, (A) uninterpreted and (B) interpreted running SW - NE in an area characterised as chaotic internal deformation. The vertical axis is in two–way travel time. See Figure 11 for location. Important reflectors have been marked on the right-hand side of both A and B, TZ (Top Zechstein), TZ3 (Top Z3), TZ2 (Top Z2), TZ1 (Top Z1) and BZ (Base Zechstein). (C) TWT depth surface (ms) of the Z3 reflector of this cross-section in a plane view, with the location of the cross-section marked in red.

Figure 9. A Seismic section (F – F') of the Zechstein from the SNSMSR2, (A) uninterpreted and (B) interpreted running SW - NE in an area characterised as area of withdrawal. The vertical axis is in two–way travel time. See Figure 11 for location. Important reflectors have been marked on the right-hand side of both A and B, TZ (Top Zechstein), TZ2 (Top Z2), TZ1 (Top Z1) and BZ (Base Zechstein).

Figure 10. A Seismic section (G – G') of the Zechstein from the SNSMSR2, (A) uninterpreted and (B) interpreted running SW - NE in an area characterised as chaotic internal deformation. The vertical axis is in two–way travel time. See Figure 11 for location. Important reflectors have been marked on the right-hand side of both A and B, TC (Top Cretaceous), TJ (Top Jurassic), TT (Top Triassic), TZ (Top Zechstein, TZ1 (Top Z1) and BZ (Base Zechstein).

Figure 11. Internal Structural Domain Map of the Zechstein in the South Permian Basin. Transects for cross sections B – G are located on the map. The 6 different characterised structural facies that have been identified in this study have been geospatially mapped using the SNSMSR2 seismic data. The identified facies can be further characterised into 3 broader domains which trend basinward.

Figure 12. Internal flow type diagram, demonstrating the different types of flow. A – E redrawn from Cartwright et al. (2012). F and G show possible flow profiles observed within the Zechstein supergroup of the United Kingdom Southern North Sea coloured to represent the different relative mechanical strength of the Zechstein Supergroup.

Figure 1.

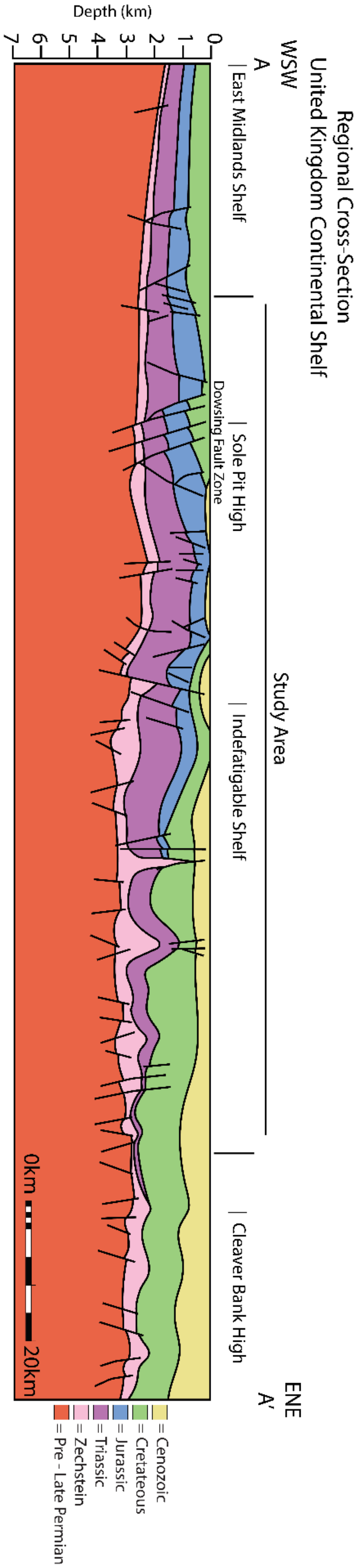

Regional Cross-Section
United Kingdom Continental Shelf
WSW
A
ENE
A'
Depth (km)
0
1
2
3
4
5
6
7
East Midlands Shelf
Sole Pit High
Dowsing Fault Zone
Study Area
Indefatigable Shelf
Cleaver Bank High
0km
20km
= Cenozoic
= Cretateous
= Jurassic
= Triassic
= Zechstein
= Pre - Late Permian

Figure 2.

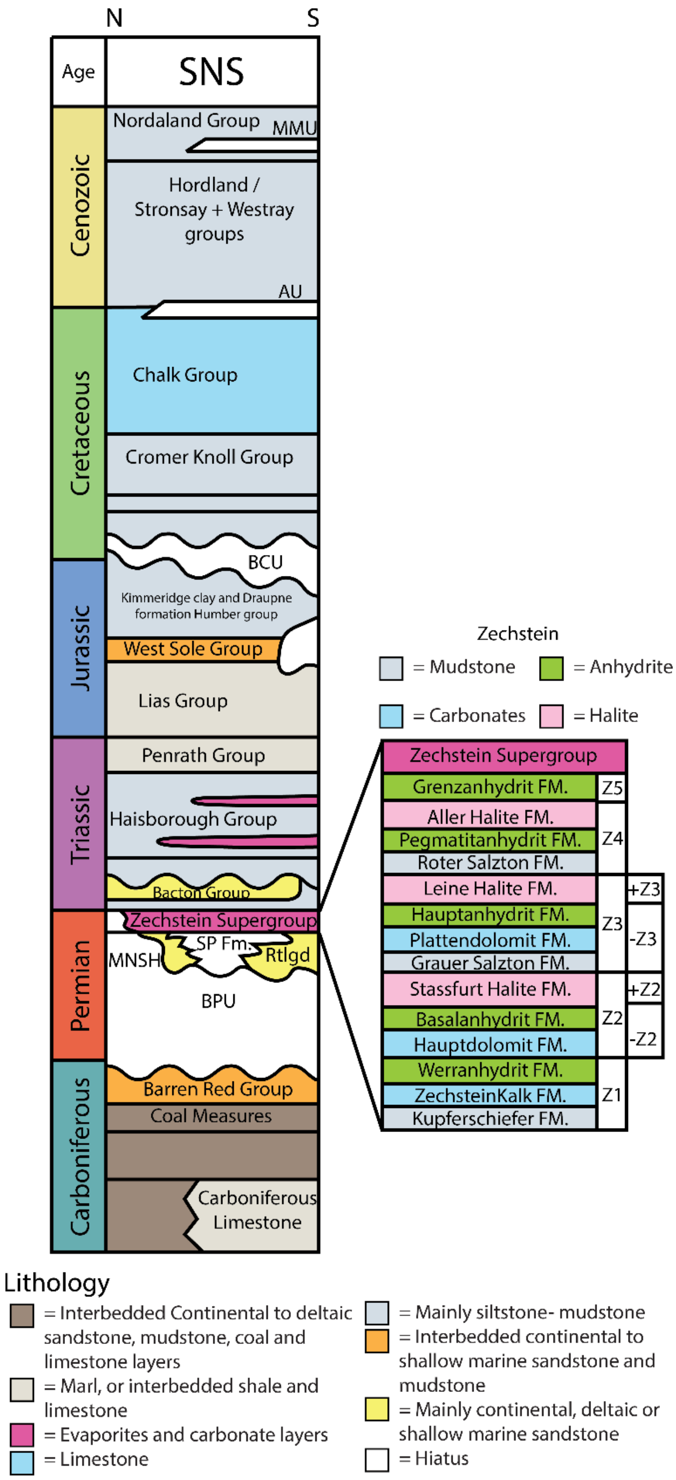

N
S
Age
SNS
Cenozoic
Nordaland Group
MMU
Hordland / Stronsay + Westray groups
AU
Cretaceous
Chalk Group
Cromer Knoll Group
Jurassic
BCU
Kimmeridge clay and Draupne formation Humber group
West Sole Group
Lias Group
Triassic
Penrath Group
Haisborough Group
Bacton Group
Permian
Zechstein Supergroup
MNSH
SP Fm.
Rtlgd
BPU
Carboniferous
Barren Red Group
Coal Measures
Carboniferous Limestone
Zechstein
= Mudstone
= Anhydrite
= Carbonates
= Halite
Zechstein Supergroup
Grenzanhydrit FM.
Z5
Aller Halite FM.
Pegmatitanhydrit FM.
Z4
Roter Salzton FM.
Leine Halite FM.
+Z3
Hauptanhydrit FM.
Z3
Plattendolomit FM.
-Z3
Grauer Salzton FM.
Stassfurt Halite FM.
+Z2
Basalanhydrit FM.
Z2
Hauptdolomit FM.
-Z2
Werranhydrit FM.
ZechsteinKalk FM.
Z1
Kupferschiefer FM.
Lithology
= Interbedded Continental to deltaic sandstone, mudstone, coal and limestone layers
= Marl, or interbedded shale and limestone
= Evaporites and carbonate layers
= Limestone
= Mainly siltstone- mudstone
= Interbedded continental to shallow marine sandstone and mudstone
= Mainly continental, deltaic or shallow marine sandstone
= Hiatus

Figure 3.

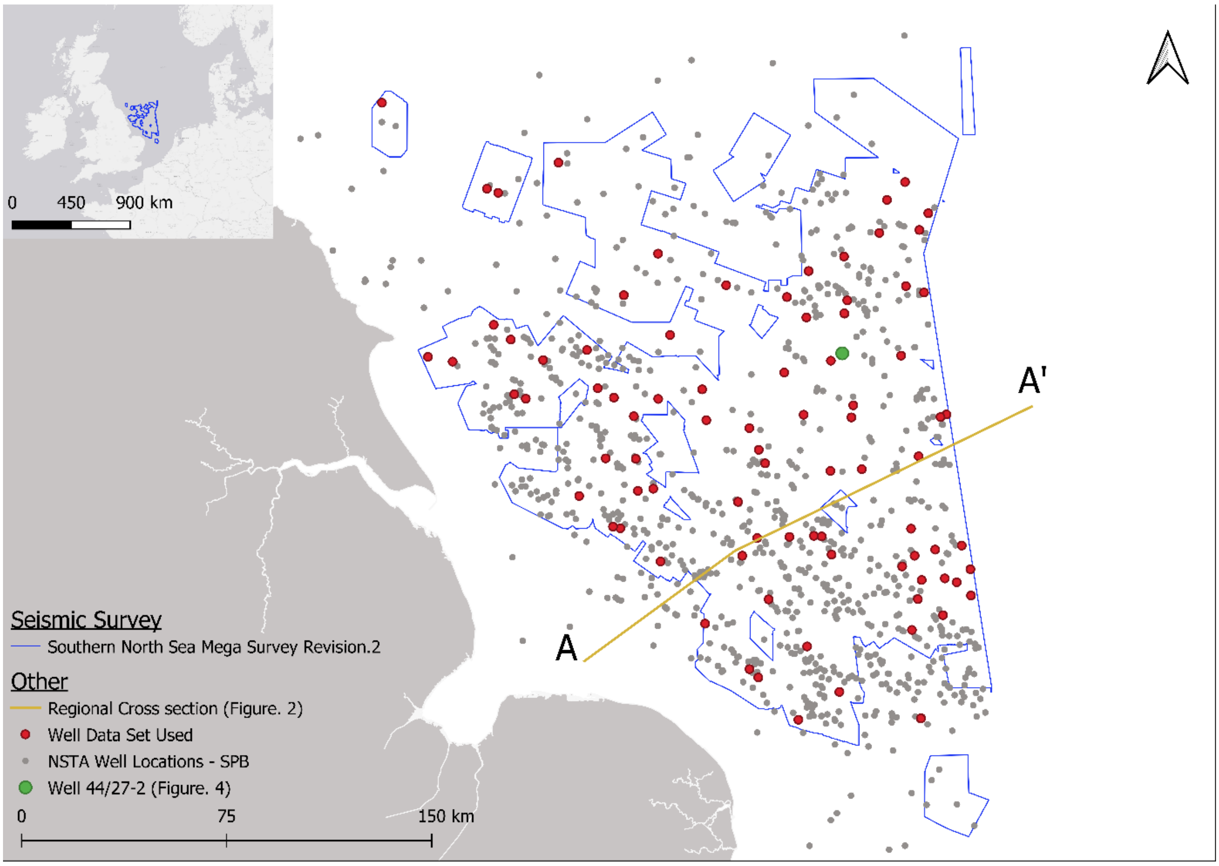
0 450 900 km
A
A'
Seismic Survey
Southern North Sea Mega Survey Revision.2
Other
Regional Cross section (Figure. 2)
Well Data Set Used
NSTA Well Locations - SPB
Well 44/27-2 (Figure. 4)
0 75 150 km

Figure. 4

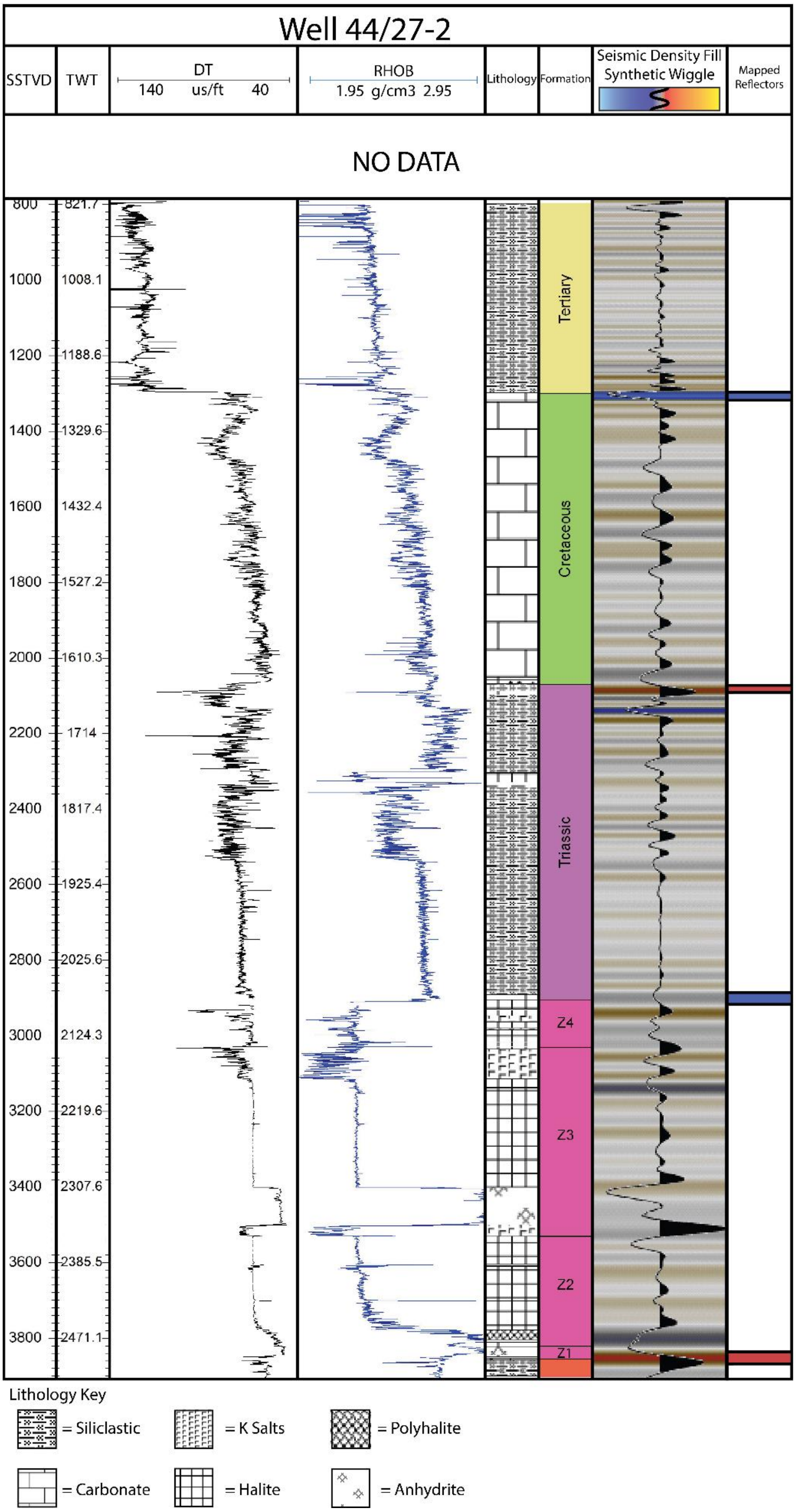

Well 44/27-2
SSTVD
TWT
DT
140 us/ft 40
RHOB
1.95 g/cm3 2.95
Lithology
Formation
Seismic Density Fill
Synthetic Wiggle
Mapped Reflectors
NO DATA
800
821.7
1000
1008.1
1200
1188.6
1400
1329.6
1600
1432.4
1800
1527.2
2000
1610.3
2200
1714
2400
1817.4
2600
1925.4
2800
2025.6
3000
2124.3
3200
2219.6
3400
2307.6
3600
2385.5
3800
2471.1
Tertiary
Cretaceous
Triassic
Z4
Z3
Z2
Z1
Lithology Key
= Siliclastic
= K Salts
= Polyhalite
= Carbonate
= Halite
= Anhydrite

884

Figure 5.

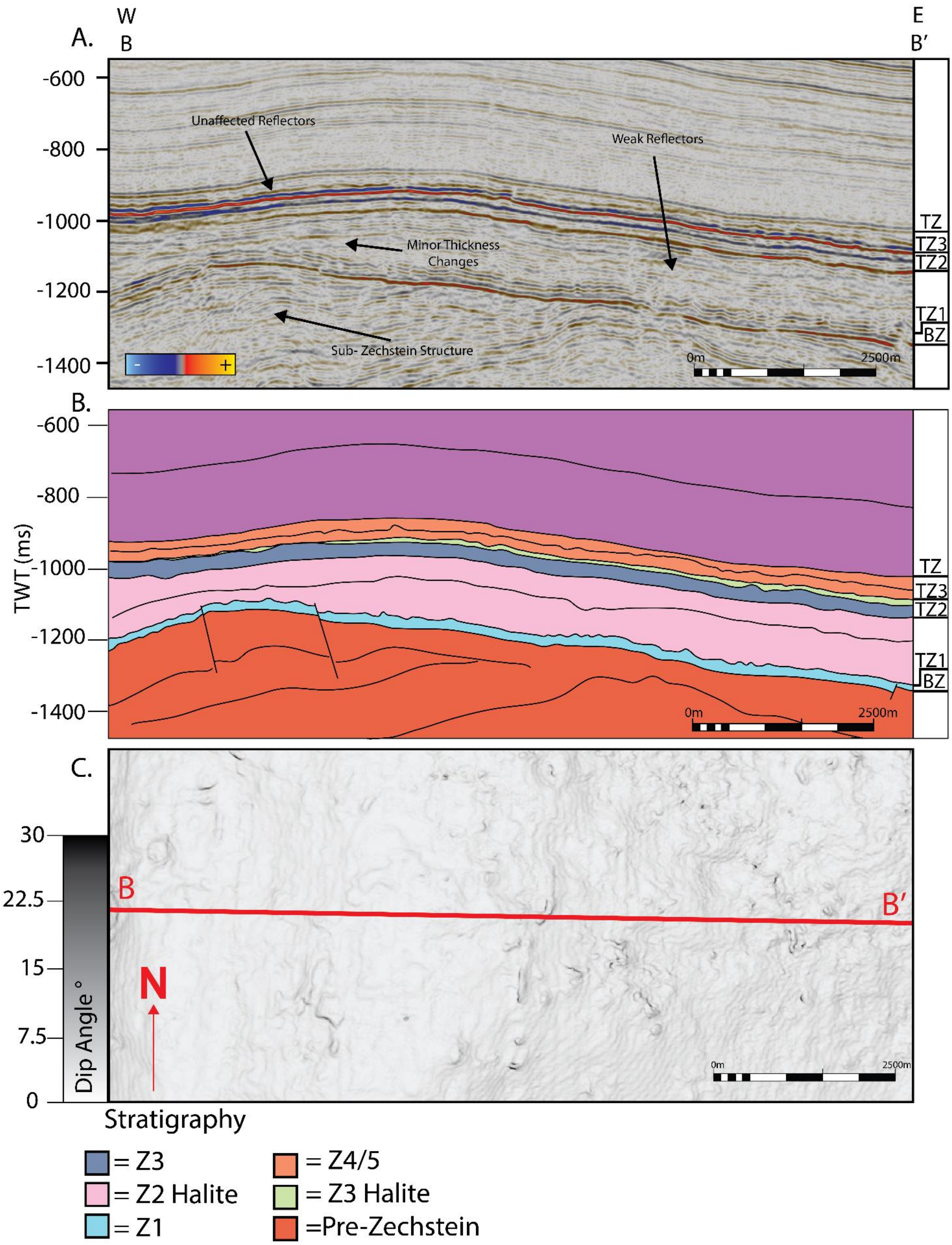

885

Figure 6.

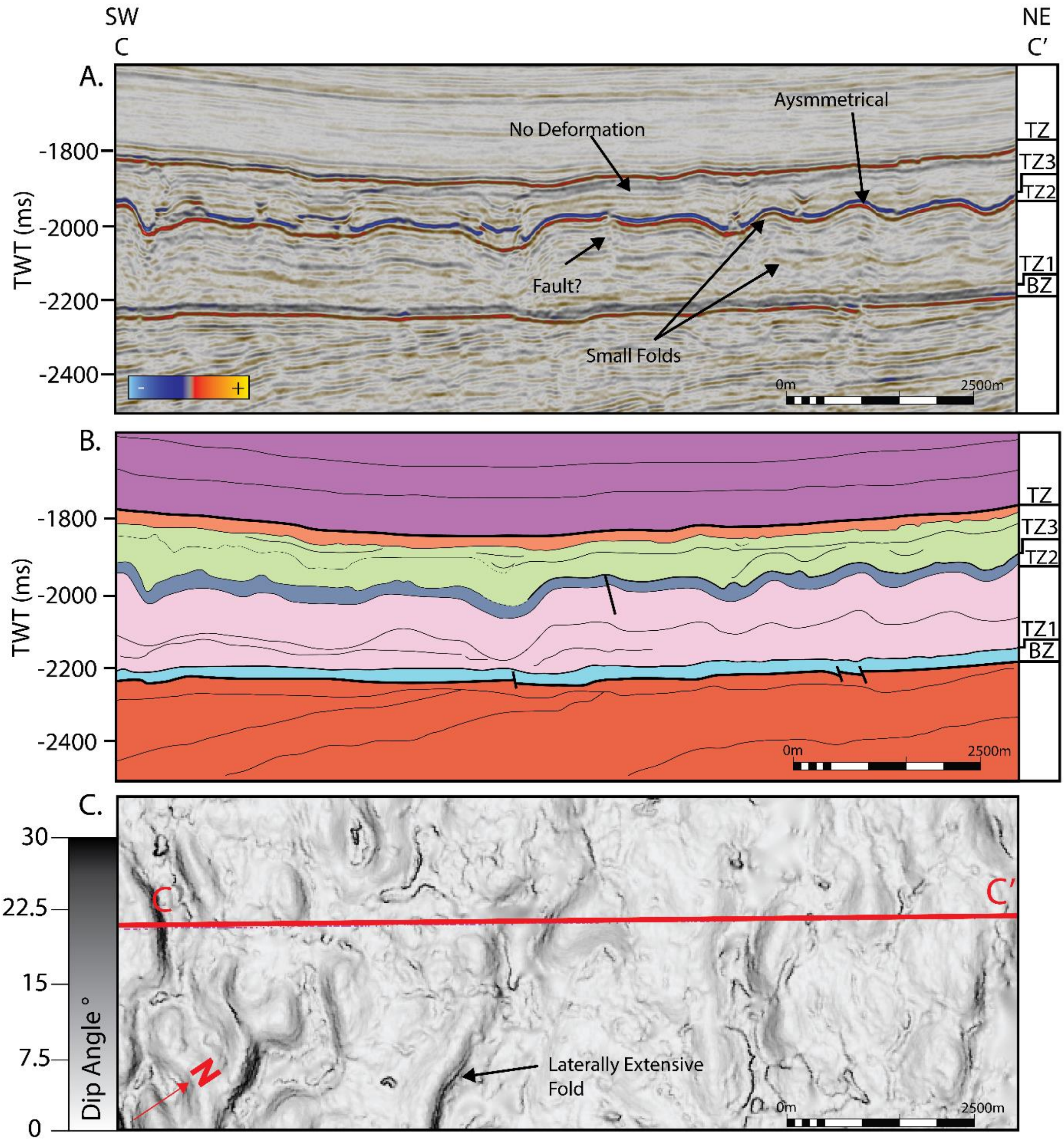

SW
C
NE
C′
A.
No Deformation
Aysmmetrical
Fault?
Small Folds
TWT (ms)
-1800
-2000
-2200
-2400
TZ
TZ3
TZ2
TZ1
BZ
0m
2500m
B.
C.
30
22.5
15
7.5
0
Dip Angle °
N
Laterally Extensive
Fold

Figure. 7

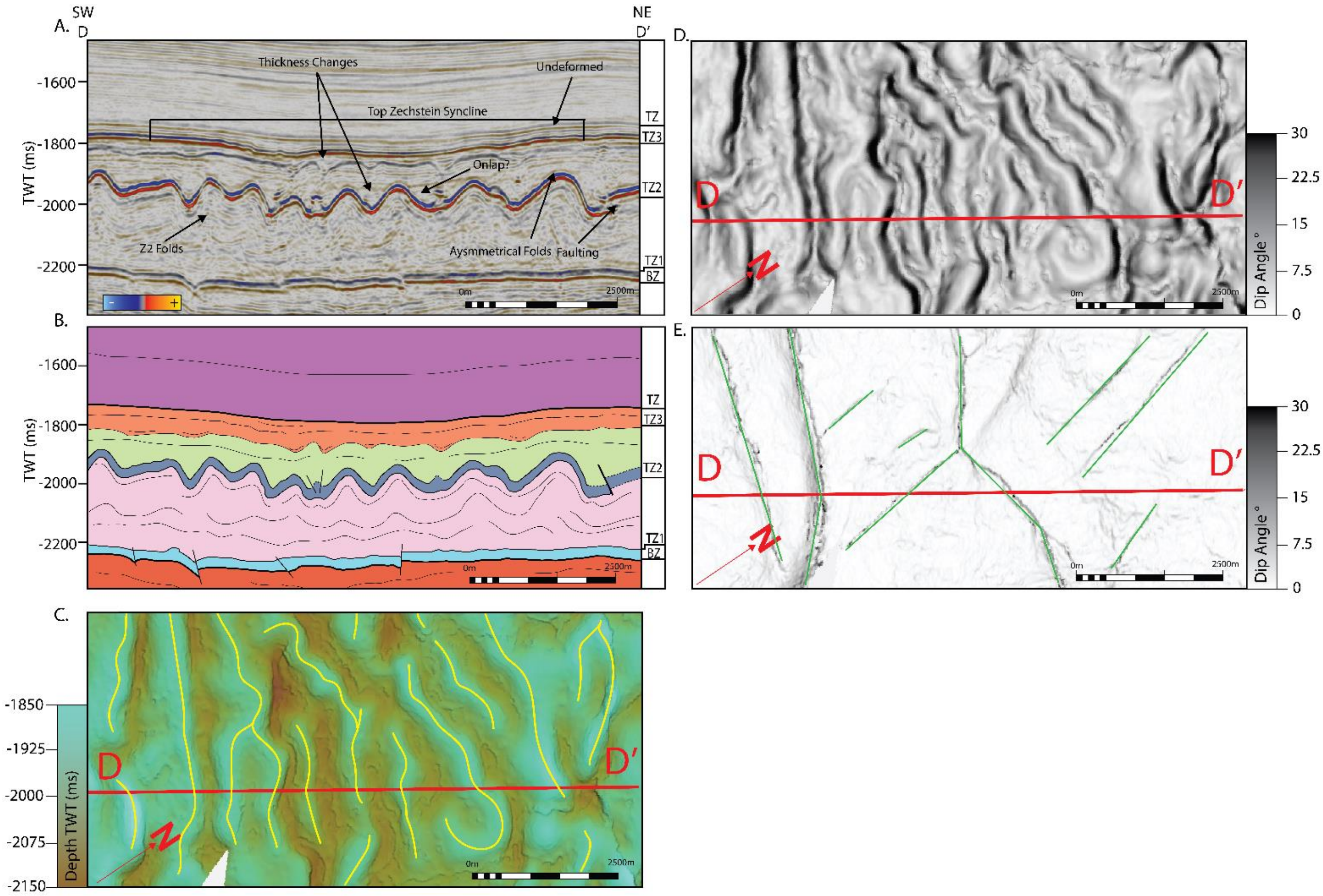

A.
SW
D
NE
D′
TWT (ms)
-1600
-1800
-2000
-2200
Thickness Changes
Undeformed
Top Zechstein Syncline
Onlap?
Z2 Folds
Aysmmetrical Folds
Faulting
TZ
TZ3
TZ2
TZ1
BZ
0m
2500m
B.
C.
-1850
-1925
-2000
-2075
-2150
Depth TWT (ms)
D
D′
N
D.
E.
Dip Angle °
30
22.5
15
7.5
0

Figure. 8

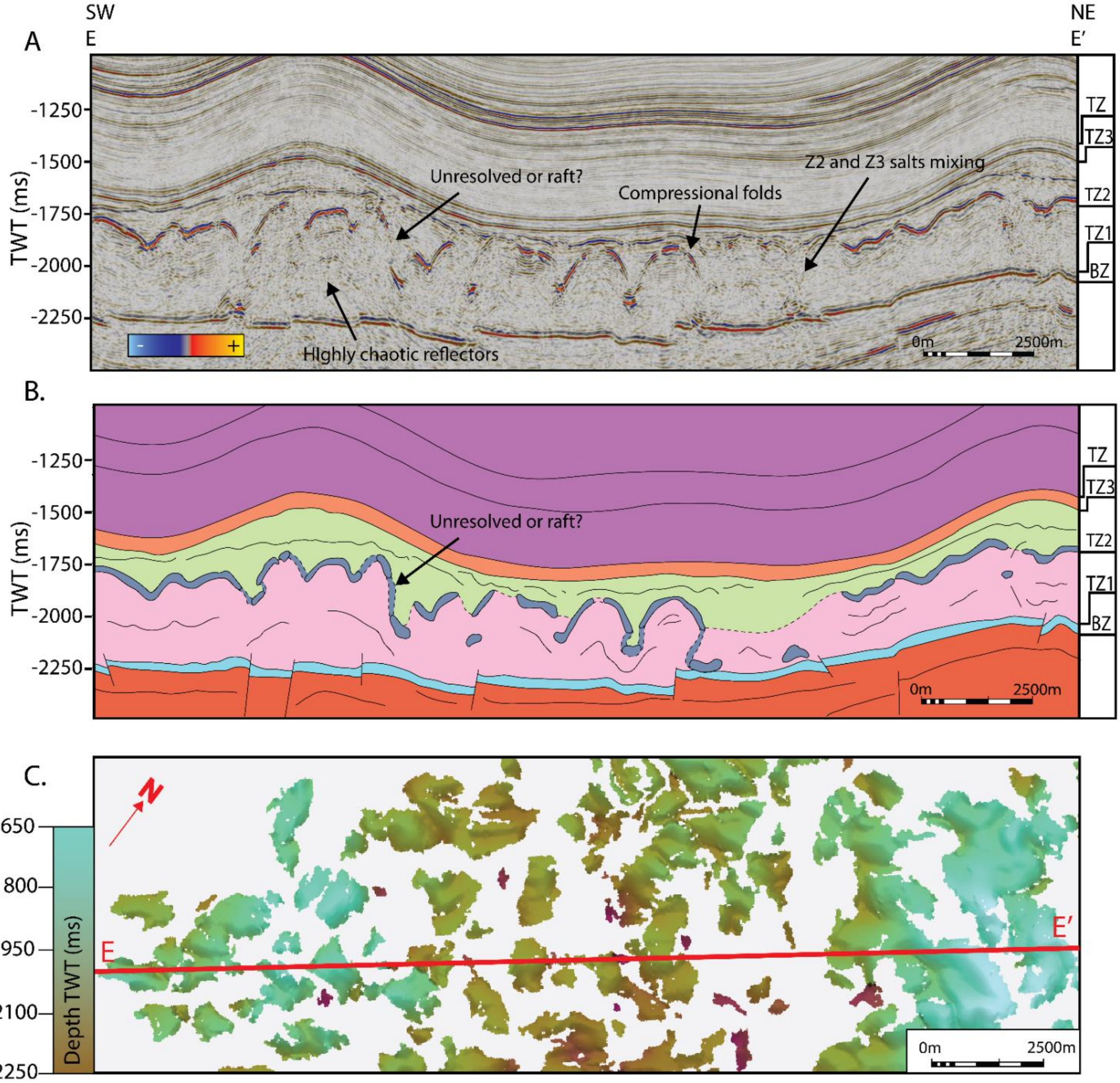

Figure 9.

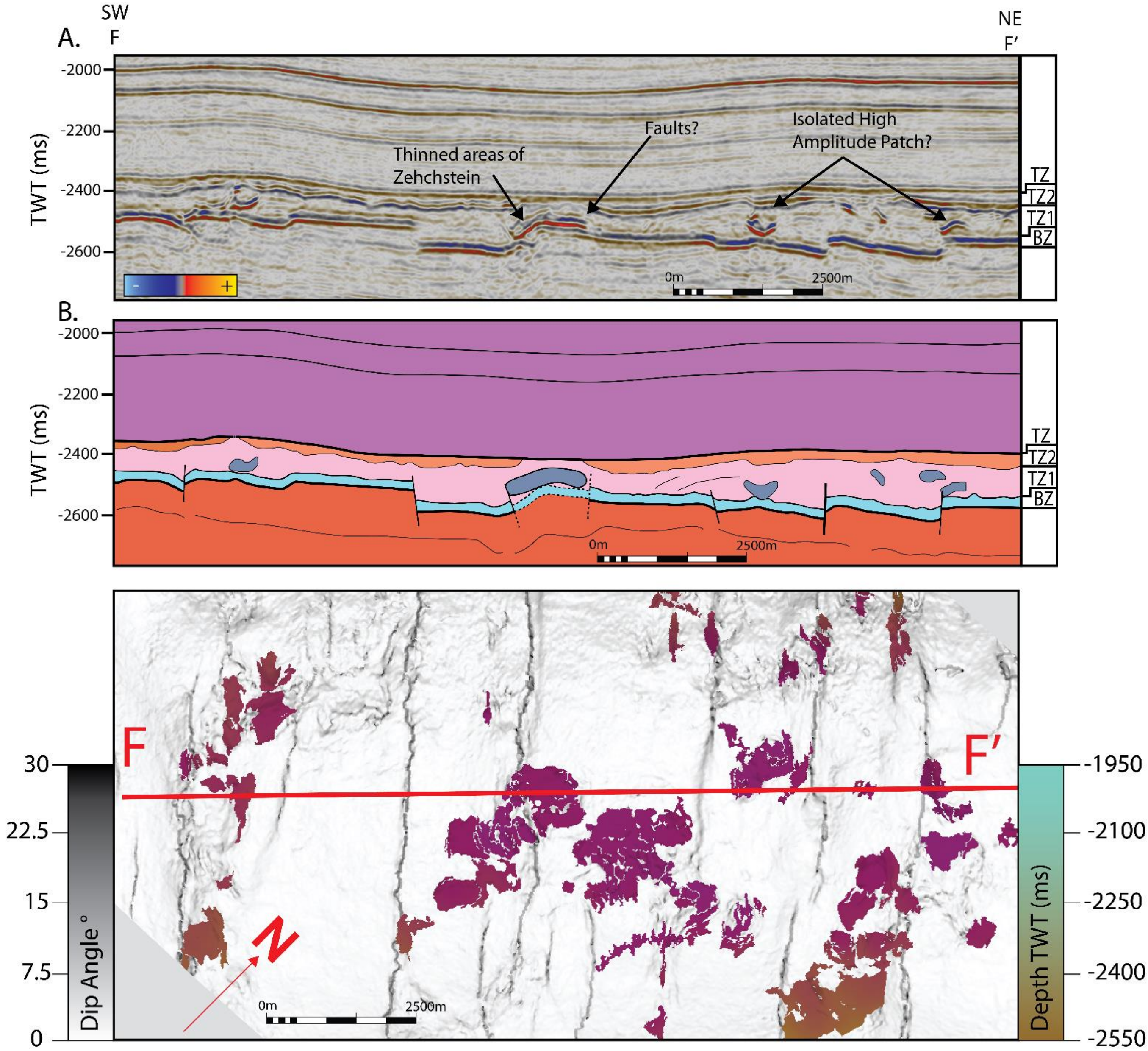
SW
F
A.
NE
F′
-2000
-2200
-2400
-2600
TWT (ms)
Thinned areas of Zehchstein
Faults?
Isolated High Amplitude Patch?
TZ
TZ2
TZ1
BZ
0m
2500m
B.
-2000
-2200
-2400
-2600
TWT (ms)
TZ
TZ2
TZ1
BZ
0m
2500m
F
F′
30
22.5
15
7.5
0
Dip Angle °
N
0m
2500m
-1950
-2100
-2250
-2400
-2550
Depth TWT (ms)

Figure. 10

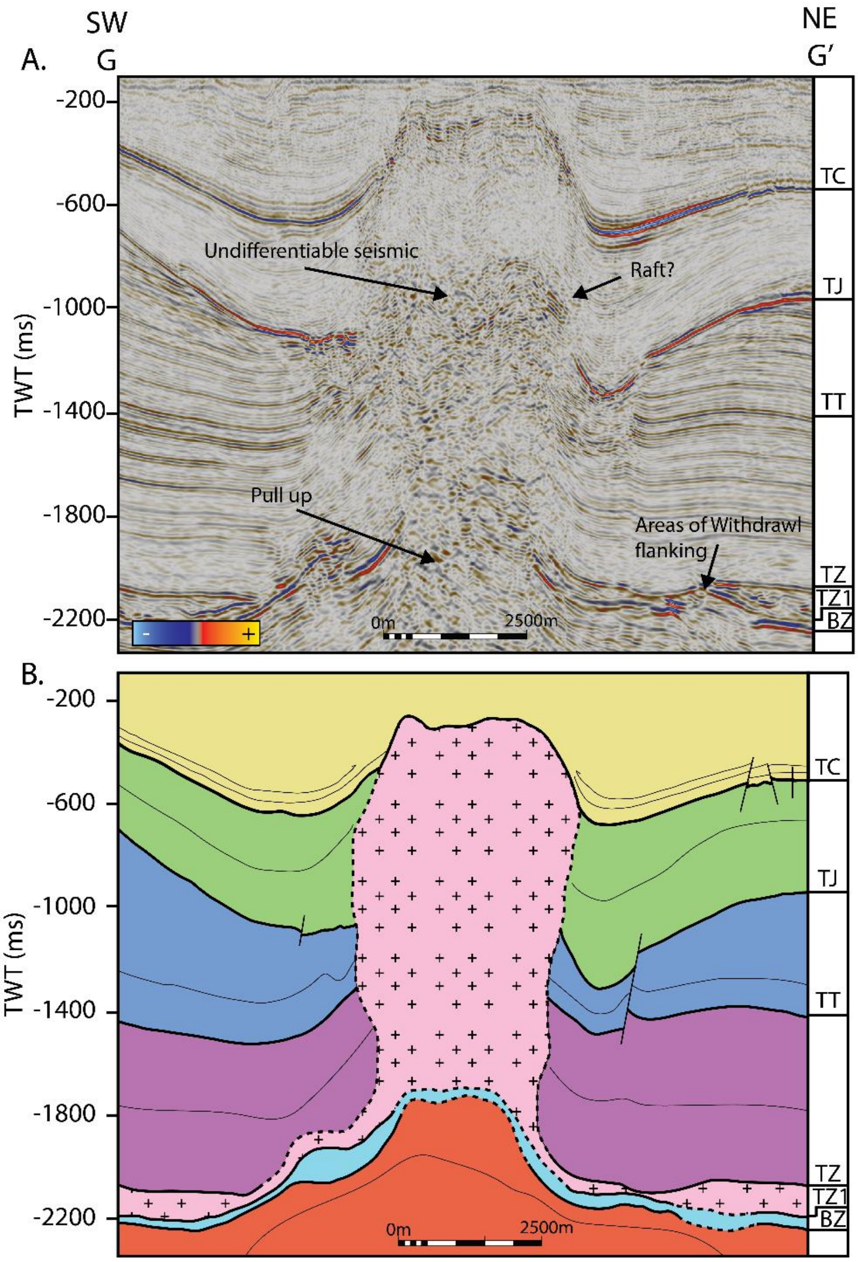
SW
G
NE
G′
A.
B.
TWT (ms)
-200
-600
-1000
-1400
-1800
-2200
Undifferentiable seismic
Raft?
Pull up
Areas of Withdrawl flanking
0m
2500m
TC
TJ
TT
TZ
TZ1
BZ

Figure. 11

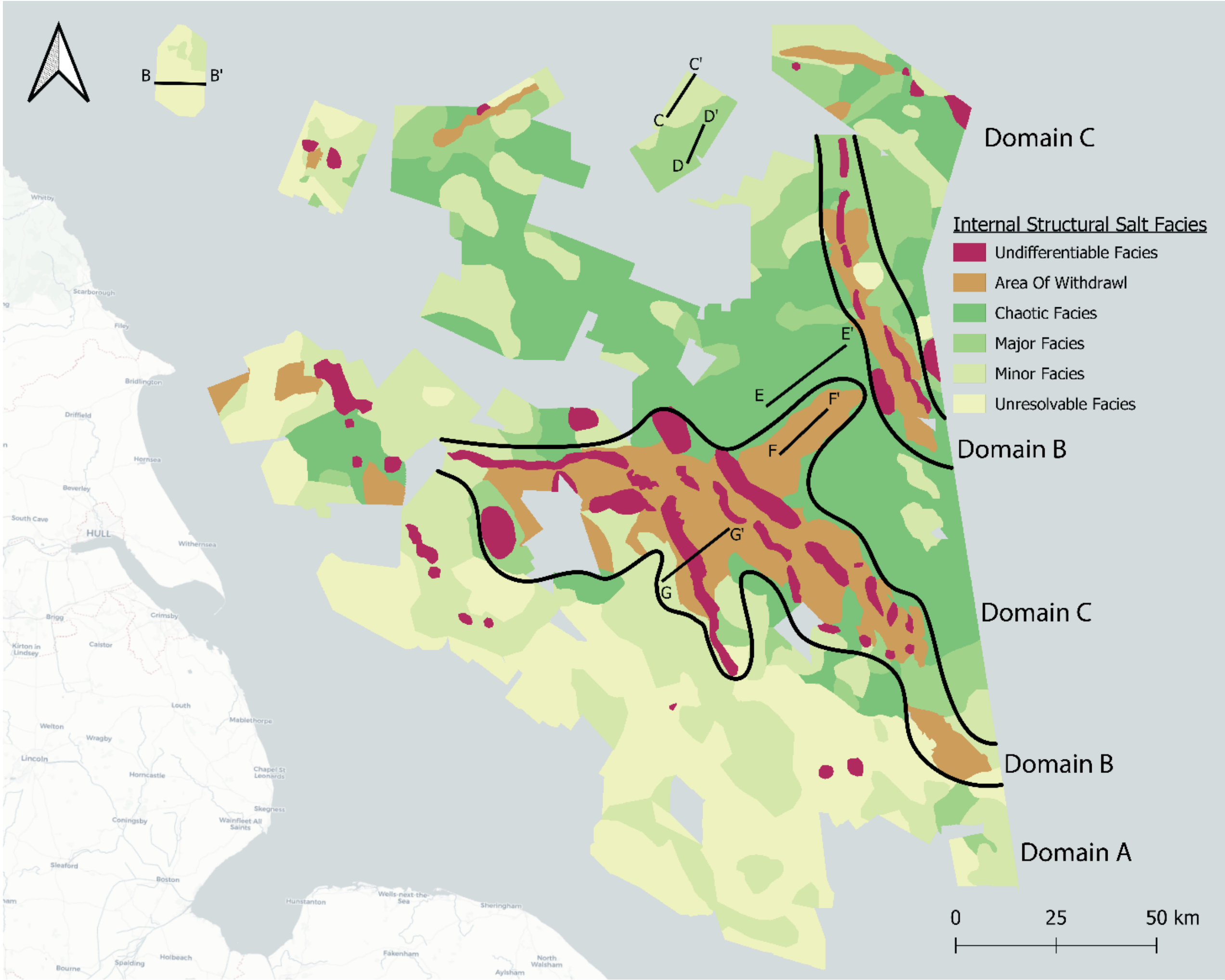
B
B'
C'
C
D'
D
Domain C
Internal Structural Salt Facies
Undifferentiable Facies
Area Of Withdrawl
Chaotic Facies
Major Facies
Minor Facies
Unresolvable Facies
E'
E
F'
F
Domain B
G'
G
Domain C
Domain B
Domain A
0
25
50 km

Figure. 12

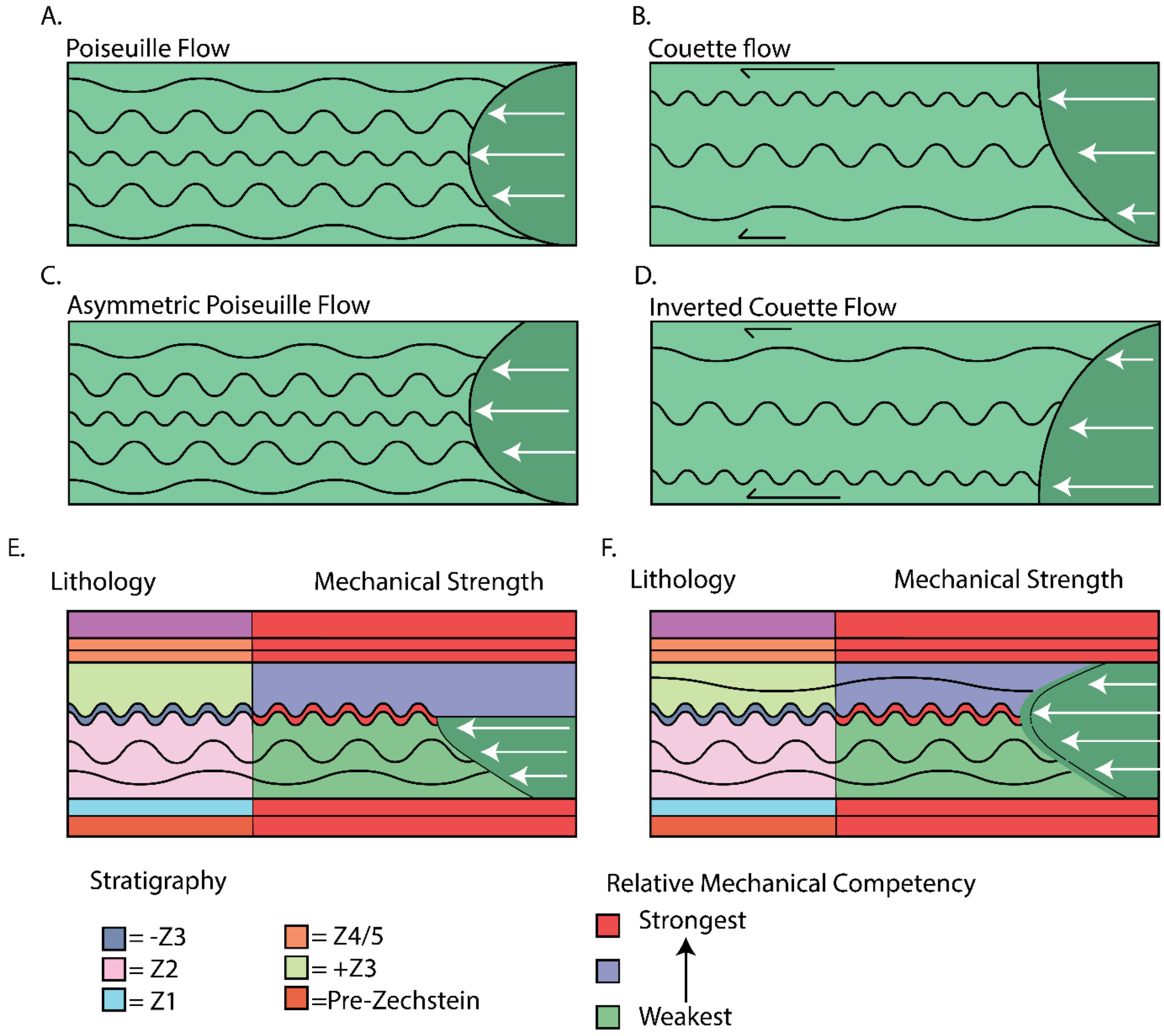

x. Data availability statement

The data that support the findings of this study are openly available in Newcastle University Data Repository [Permant Link to be added]. The Seismic data and well data used within this study are available from the North Sea Transition Authority's National Data Repository (https://ndr.nstauthority.co.uk/). The bathymetry data used within this paper is available from European Martine Observation and Data Network (EMODnet) (https://portal.emodnet-bathymetry.eu/).

xi. ORCID

Hector Barnett - https://orcid.org/0000-0003-2506-5524

Mark T Ireland - https://orcid.org/0000-0001-9777-0447

Cees van der Land - https://orcid.org/0000-0002-0301-6927

xii. Appendix

Supplementary Table A. List of wells used within this paper.

Wells Used
41/5-1
42/15a-3
42/26-1
42/27a-1
42/28a-6
42/28b-5
42/29-2
42/30-4A
43-7-1
43/17-2
43/21b-5Z
43/23-2
43/24-2
43/28a-3
43/30-1
44/13-1
44/14-1
44/14-2
44/18-1
44/19-2
44/19a-5
44/21-1
44/21a-5
44/21B-8
44/22-5
44/22b-8
44/24-2
44/24a-5
44/26c-6

44/27-1
44/27-2
44/28-3
47/15-1
47/3-1
47/4a-7
48-11b-5
48/03-1
48/1-2A
48/10-1
48/10b-10
48/10c-11
48/11-2
48/12b-03
48/12e-11
48/14-2
48/17-1
48/17a-9
48/19A- 4
48/1a-3
48/20-1
48/23-2
48/25-1
48/2b-3
48/2c-5
48/3-2
48/30-1
48/30-6
48/3a-5
48/6-10
48/7-1
49/1-1
49/14a-2
49/16-12
49/16-6
49/17-4
49/17-9
49/19-1
49/19-3
49/19-7
49/2-2
49/2-3
49/20-2
49/20a-8

49/20b-3
49/20b-4
49/24- 2
49/24-12
49/25a-5
49/26- 2
49/5-2
49/5-5
49/7a-1
49/8-1
49/9-1
50/16-1
50/21-1
53/04-1
53/1b-12
53/2-2
49/16-5
43/10-1
48/11-1
42/13-4
42/13-2
44/29-2
44/17-1

948